To be submitted to ApJ.

Final Results from an Adaptive Optics Imaging Survey for Giant Planets Orbiting Nearby Sunlike Stars in the L' and M-bands.

A. N. Heinze

Swarthmore College, 500 College Avenue, Swarthmore, PA 19081

aheinze1@swarthmore.edu

Philip M. Hinz

Steward Observatory, University of Arizona, 933 N Cherry Avenue, Tucson, AZ 85721-0065

phinz@as.arizona.edu

Matthew Kenworthy

Steward Observatory, University of Arizona, 933 N Cherry Avenue, Tucson, AZ 85721-0065

mkenworthy@as.arizona.edu

Michael Meyer

Steward Observatory, University of Arizona, 933 N Cherry Avenue, Tucson, AZ 85721-0065

mmeyer@as.arizona.edu

Suresh Sivanandam

Steward Observatory, University of Arizona, 933 N Cherry Avenue, Tucson, AZ 85721-0065

suresh@as.arizona.edu

Douglas Miller

Steward Observatory, University of Arizona, 933 N Cherry Avenue, Tucson, AZ 85721-0065

dlmiller@as.arizona.edu

ABSTRACT

[1]Observations reported here were obtained at the MMT Observatory, a joint facility of the University of Arizona and the Smithsonian Institution.

We report the final results of an Adaptive Optics (AO) imaging survey of 54 nearby, sunlike stars for extrasolar planets, carried out in the L' and M bands using the Clio camera on the MMT. This survey concentrates more strongly than all others to date on very nearby F, G, and K stars, in that proximity is prioritized higher than youth. It is also the first survey to include extensive observations in the M band, which supplemented the primary L' observations. These longer wavelengths are most useful for very nearby systems in which low temperature planets with red IR colors (i.e. $H - L'$, $H - M$) could be detected. A previously unknown $\sim 0.15 M_{\odot}$ stellar companion to the F9 star GJ 3876 was discovered at a projected separation of about 80 AU, but no planets were found. Extensive Monte Carlo simulations allow us to interpret this null result into constraints on the distribution of extrasolar planets. If the distribution of planets is a power law with $dN \propto M^{\alpha} a^{\beta} dM da$, normalized to be consistent with radial velocity statistics, we find that $\alpha = -1.1$ and $\beta = -0.44$, truncated at 100 AU, is ruled out at the 90% confidence level. With 90% confidence no more than 8.1% of stars like those in our survey have systems with three widely spaced, massive planets like the A-star HR 8799. While surveys targeting younger stars at shorter wavelengths have set tighter limits, our observations confirm that a paucity of giant planets at wide separations around sun-like stars is also seen in mature systems, and is robustly observed with AO surveys at a range of wavelengths.

Subject headings: planetary systems, techniques: IR imaging, intrumentation: adaptive optics, astrometry, binary stars

1. Introduction

Well over 200 extrasolar planets have now been discovered using the radial velocity (RV) method. The limited temporal baseline of radial velocity observations, and the need to observe for a complete orbital period to confirm the properties of a planet with confidence, currently limit RV planets to periods of about 10 years or less. The masses of discovered planets range from just a few Earth masses (Bouchy et al. 2009) up to around 20 Jupiter masses (MJ). We note that a 20 MJ object would be considered by many to be a brown dwarf rather than a planet, but that there is no broad consensus on how to define the upper mass limit for planets. For a good overview of RV planets to date, see Butler et al. (2006) or http://exoplanet.eu/catalog-RV.php.

The large number of RV planets makes it possible to examine the statistics of extrasolar planet populations. Several groups have fit approximate power law distributions in mass and semimajor axis to the set of known extrasolar planets. Necessarily, however, these power laws are not subject to observational constraints at orbital periods longer than 10 years – and it is at these orbital periods that we find giant planets in our own solar system. We cannot obtain a good understanding of planets in general without information on long period extrasolar planets. Nor can we see how our

own solar system fits into the big picture of planet formation in the galaxy without a good census of planets in Jupiter- and Saturn-like orbits around other stars.

Repeatable detections of extrasolar planets (as opposed to one-time microlensing detections) have so far been made by transit detection, by RV variations, by astrometric wobble, or by direct imaging. Of these methods, transits are efficient only for detecting close-in planets. The RV method is currently limited (by the amount of time high-precision spectrographs have been operating) to planets with periods of about 10 years or less, but even as temporal baselines increase, long period planets will remain harder to detect due to their slow orbital velocities. The amplitude of a star's astrometric wobble increases with the radius of its planet's orbit, but decades-long observing programs are still needed to find long-period planets. Direct imaging is the only method that allows us to characterize long-period extrasolar planets immediately.

Direct imaging of extrasolar planets is technologically possible at present only in the infrared, based on the planets' own thermal luminosity, not on reflected starlight. The enabling technology is adaptive optics (AO), which allows 6-10m ground-based telescopes to obtain diffraction limited IR images several times sharper than those from HST, despite Earth's turbulent atmosphere. Theoretical models of giant planets indicate that such telescopes should be capable of detecting self-luminous giant planets in large orbits around young, nearby stars. The stars should be young because the glow of giant planets comes from gravitational potential energy converted to heat in their formation and subsequent contraction: lacking any internal fusion, they cool and become fainter as they age.

Several groups have published the results of AO imaging surveys for extrasolar planets around F, G, K, or M stars in the last five years (see for example Masciadri et al. (2005); Kasper et al. (2007); Biller et al. (2007); Lafrenière et al. (2007). Of these, most have used wavelengths in the 1.5-2.2 μm range, corresponding to the astronomical H and K_S filters (Masciadri et al. 2005; Biller et al. 2007; Lafrenière et al. 2007). They have targeted mainly very young stars. Because young stars are rare, the median distance to stars in each of these surveys has been more than 20 pc.

In contrast to those above, our survey concentrates on very nearby F, G, and K stars, with proximity prioritized more than youth in the sample selection. The median distance to our survey targets is only 11.2 pc. Ours is also the first survey to include extensive observations in the M band, and only the second to search solar-type stars in the L' band (the first was Kasper et al. (2007)). The distinctive focus on older, very nearby stars for a survey using longer wavelengths is natural: longer wavelengths are optimal for lower temperature planets which are most likely to be found in older systems, but which would be undetectable around all but the nearest stars.

Our survey places constraints on a more mature population of planets than those that have focused on very yong stars, and confirms that a paucity of giant planets at large separations from sun-like stars is robustly observed at a wide range of wavelengths.

In Section 2 we describe the criteria used in choosing our sample, and present the characteristics of our stars. In Section 3, we briefly describe our instrument, out observing strategy, and our image

processing pipeline. In Section 4 we detail our sensitivity estimation methods, and show how we characterized them using blind tests in which simulated planets were inserted into our raw data – a practice that should be standard for planet imaging surveys. In Section 5 we give astrometric and photometric data for all faint companions detected in our survey (note that astrometric information on bright binary stars in our sample is also provided in Table 14).

In Section 6, we review power law fits to the distribution of known RV planets, including the normalization of the power laws. In Section 7, we present the constraints our survey places on the distribution of extrasolar giant planets, based on extensive Monte Carlo simulations. In Section 8 we discuss the promising future of planet-search observations in the L' and especially the M band, and in Section 9 we conclude.

2. The Survey Sample

The goal of our sample selection was to pick the nearest stars around which we could detect planets of 10 Jupiter Masses (MJ) or below. This practically meant that very nearby stars were potential targets up to ages of several Gyr, while at larger distances we would consider only fairly young stars. We set out initially to investigate only FGK stars within 25pc of the sun, in order to make our sample comparable in spectral type to the samples of the RV surveys and to focus on the nearest stars, at which the L' and M bands are most useful relative to shorter wavelengths. In the end we included a few M stars and a few stars slightly beyond 25pc, because these stars were very interesting and we had exhausted most of the observable stars that lay within our more strict criteria. The stars of our sample are presented in Table 2.

Our survey focuses on markedly more nearby stars than all other surveys published to date. For example, the median distance to stars in the Masciadri et al. (2005) survey is 21.2 pc. For the Kasper et al. (2007) survey the median distance is 37 pc, for Biller et al. (2007) it is 24.7 pc, and for Lafrenière et al. (2007) it is 21.7 pc. Our median distance is 11.2 pc.

Table 1. Age, Distance, and Spectral Type of Survey Targets

Star	Age 1 (Gyr)	Age 2 (Gyr)	Adopted Age (Gyr)	Dist. (pc)	Spectral Type
GJ 5	0.11[a]	0.2[b]	0.155	14.25	K0Ve
HD 1405	0.1-0.2[c]	0.03-0.08[d]	0.1	30	K2V
τ Ceti	···	···	5	3.50	G8Vp
GJ 117	0.1[c]	0.03[a]	0.1	8.31	K2V
ϵ Eri	0.56[a]	···	0.56	3.27	K2V
GJ 159	0.03-0.01[e]	···	0.1	18.12	F6V
GJ 166 B	···	···	2	4.83	DA
GJ 166 C	···	···	2	4.83	dM4.5e
HD 29391	0.01-0.03[f]	···	0.1	14.71	F0V
GJ 211	0.52[a]	···	0.52	12.09	K1Ve
GJ 216 A	0.4-0.6[g]	···	0.44	8.01	F6V
BD+20 1790	0.06-0.3[e]	···	0.18	24	K3
GJ 278 C	0.1-0.3[h]	···	0.2	14.64	M0.5Ve
GJ 282 A	0.49[a]	0.4-0.6[g]	0.5	13.46	K2Ve
GJ 311	0.1[c]	0.1-0.3[e]	0.24	13.85	G1V
HD 77407 A	0.05[i]	···	0.1	30.08	G0V
HD 77407 B	0.05[i]	···	0.1	30.08	M2V
HD 78141	0.1-0.2[c]	···	0.15	21.4	K0
GJ 349	0.37[a]	···	0.37	11.29	K3Ve
GJ 355	0.1[c]	0.05-0.15[j]	0.1	19.23	K0
GJ 354.1 A	0.1[c]	0.02-0.15[j]	0.1	18.87	dG9
GJ 380	···	···	2	4.69	K2Ve
GJ 410	0.2-0.6[g]	···	0.37	11	dM2e
HD 96064 A	0.1-0.2[c]	···	0.15	24.63	G5V
HD 96064 B	0.1-0.2[c]	···	0.15	24.63	M3V
GJ 450	<1.0[k]	···	1	8.1	M1Ve
BD+60 1417	0.1-0.2[c]	···	0.15	17.7	K0
HD 113449	0.1-0.2[c]	···	0.15	22.1	G5V
GJ 505 A	0.79[a]	···	0.79	11.9	K2V
GJ 505 B	0.79[a]	···	0.79	11.9	M0.5V
GJ 519	0.2-0.6[g]	···	0.37	9.81	dM1
GJ 3860	0.28[a]	0.2-0.6[g]	0.28	14.93	K0

Table 1—Continued

Star	Age 1 (Gyr)	Age 2 (Gyr)	Adopted Age (Gyr)	Dist. (pc)	Spectral Type
GJ 564	0.1-0.2[c]	···	0.15	17.94	G2V
GJ 3876	···	···	2	43.3	F9IV
ξ Boo A	0.43[a]	0.1[c]	0.29	6.71	G8V
ξ Boo B	0.15[a]	···	0.29	6.71	K4V
HD 139813	0.1-0.2[c]	···	0.15	21.7	G5
GJ 625	0.4-0.6[g]	···	0.5	6.28	dM2
GJ 659 A	<1.0[l]	···	1	20.2	K8V
GJ 659 B	<1.0[l]	···	1	20.2	dK8
GJ 684 A	0.4-0.6[g]	···	0.5	14.09	G0V
GJ 684 B	0.4-0.6[g]	···	0.5	14.09	K3V
GJ 702 A	···	···	2	5.03	K0V
GJ 702 B	···	···	2	5.03	K4V
61 Cyg A	···	···	2	3.46	K5V
61 Cyg B	···	···	2	3.46	K7V
BD+48 3686	0.1-0.2[c]	···	0.15	23.6	K0
GJ 860 A	<1.0[k]	···	1	4.01	M2V
GJ 860 B	<1.0[k]	···	1	4.01	M6V
GJ 879	0.1-0.3[h]	···	0.2	7.81	K5Ve
HD 220140 A	0.025-0.15[j]	···	0.1	19.74	G9V
HD 220140 B	0.025-0.15[j]	···	0.1	19.74	G9V
GJ 896 A	<0.3[h]	···	0.3	6.58	M3.5
GJ 896 B	<0.3[h]	···	0.3	6.58	M4.5

Note. — The adopted age, usually an average of the referenced values, is the age we used in our Monte Carlo simulations.

[a]Fischer (1998)

[b]Bryden et al. (2006)

[c]Wichmann et al. (2003)

[d]López-Santiago et al. (2006)

[e]Age estimate from FEPS target list, courtesy M. Meyer.

[f]Zuckerman et al. (2001)

[g]King et al. (2003)

[h]Barrado y Navascués (1998)

[i]Wichmann & Schmitt (2003)

[j]Montes et al. (2001)

[k]The Hünsch et al. (1998) catalog reports a ROSAT detection at a flux level that suggests an age of 1 Gyr or less.

[l]Favata et al. (1998)

Surveying nearby, older stars at long wavelengths is interesting for several reasons. First, nearby stars offer the best chance to see planets at small physical separations, perhaps even inward to the outer limits of RV sensitivity. Second, planetary systems with ages up to several hundred Myr may still be undergoing substantial dynamical evolution due to planet-planet interactions (Juric & Tremaine 2007; Gomes et al. 2005). While finding systems in the process of dynamical evolution would be fascinating, we also need information about systems old enough to have settled down into a mature, stable configuration. To probe long-period planet populations in mature systems, surveys such as ours that target older stars are necessary.

Additionally, theoretical spectra of older planets are likely more reliable than for younger ones, as these planets are further from their unknown starting conditions and moving toward a well-understood, stable configuration such as Jupiter's. It has been suggested by Marley et al. (2007), in fact, that theoretical planet models such as those of Burrows et al. (2003) may overpredict the brightness of young ($<$ 100 Myr) planets by orders of magnitude, while for older planets the models are more accurate. Lastly, L' surveys such as ours and that of Kasper et al. (2007) are an important complement to the shorter-wavelength work of Masciadri et al. (2005); Biller et al. (2007); and Lafrenière et al. (2007) in that they insure that limits on planet populations do not depend entirely on yet-untested predictions of the flux from extrasolar giant planets in a narrow wavelength interval. Until a sufficient number of extrasolar planets have been directly imaged that their spectra are well understood, surveys conducted at a range of different wavelengths will increase the confidence that may be placed in the results.

Table 2. Position and Magnitude of Survey Targets

Star	RA	DEC	V	H	K	L'
GJ 5	00:06:36.80	29:01:17.40	6.13	4.69	4.31	4.25
HD 1405	00:18:20.90	30:57:22.00	8.60	6.51	6.39	6.32
τ Ceti	01:44:04.10	-15:56:14.90	3.50	1.77	1.70	1.65
GJ 117	02:52:32.10	-12:46:11.00	6.00	4.23	4.17	4.11
ϵ Eri	03:32:55.80	-09:27:29.70	3.73	1.88	1.78	1.72
GJ 159	04:02:36.70	-00:16:08.10	5.38	4.34	4.18	4.14
GJ 166 B	04:15:21.50	-07:39:22.30	9.50	...	...	...
GJ 166 C	04:15:21.50	-07:39:22.30	11.17	5.75	5.45	5.05
HD 29391	04:37:36.10	-02:28:24.80	5.22	4.77	4.54	4.51
GJ 211	05:41:20.30	53:28:51.80	6.23	3.99	4.27	4.21
GJ 216 A	05:44:27.80	-22:26:54.20	3.60	2.47	2.42	2.38
BD+20 1790	07:23:43.60	20:24:58.70	9.93	7.61	7.51	7.42
GJ 278 C	07:34:37.40	31:52:09.80	9.07	5.42	5.24	5.05
GJ 282 A	07:39:59.30	-03:35:51.00	7.20	5.06	4.89	4.82
GJ 311	08:39:11.70	65:01:15.30	5.65	4.28	4.17	4.12
HD 77407 A	09:03:27.10	37:50:27.50	7.10	5.53	5.44	5.39
HD 77407 B	09:03:27.10	37:50:27.50	...	...	...	...
HD 78141	09:07:18.10	22:52:21.60	7.99	5.92	5.78	5.72
GJ 349	09:29:54.80	05:39:18.50	7.22	5.00	4.79	4.70
GJ 355	09:32:25.60	-11:11:04.70	7.80	5.60	5.45	5.39
GJ 354.1 A	09:32:43.80	26:59:18.70	7.01	5.24	5.12	5.06
GJ 380	10:11:22.10	49:27:15.30	6.61	3.93	2.96	2.89
GJ 410	11:02:38.30	21:58:01.70	9.69	5.90	5.69	5.46
HD 96064 A	11:04:41.50	-04:13:15.90	7.64	5.90	5.80	5.75
HD 96064 B	11:04:41.50	-04:13:15.90	...	...	...	...
GJ 450	11:51:07.30	35:16:19.30	9.78	5.83	5.61	5.40
BD+60 1417	12:43:33.30	60:00:52.70	9.40	7.36	7.29	7.23
HD 113449	13:03:49.70	-05:09:42.50	7.69	5.67	5.51	5.46
GJ 505 A	13:16:51.10	17:01:01.90	6.52	4.58	4.38	4.31
GJ 505 B	13:16:51.10	17:01:01.90	9.80	5.98	5.75	5.43
GJ 519	13:37:28.80	35:43:03.90	9.07	5.66	5.49	5.28
GJ 3860	14:36:00.60	09:44:47.50	7.51	5.63	5.55	5.49
GJ 564	14:50:15.80	23:54:42.60	5.88	4.47	4.42	4.37

As can be seen from Table 2, some estimates have placed the ages of some of our stars well below 100 Myr. We have chosen to approximate these ages as 100 Myr. There are several reasons for this. First, the Burrows et al. (2003) models we have adopted do not give the type of observables we need for planets younger than 100 Myr. Second, setting the ages of these stars slightly older than they are thought to be fits in with our generally conservative approach to the volatile subject of extrasolar planet searches, and ensures that our survey results do not hang on just a few very young stars and will not be invalidated if the age estimates are revised upward. Finally, setting the ages conservatively hedges our results to some extent against the possibility suggested in Marley et al. (2007) that young massive planets may be far fainter than expected because much of the gravitational potential energy of the accreting material may get radiated away in an accretion shock and thus never get deposited in the planet's interior. Figure 4 in Marley et al. (2007) shows that in this accretion scenario planets start out at much lower luminosities than predicted by 'hot start' models such as those of Burrows et al. (2003), but over time the predictions converge. By 100 Myr, the differences are less than an order of magnitude for planets less massive than 10 MJ, and are negligible for planets of 4 MJ and lower masses.

3. Observations and Image Processing

3.1. The Instrument

The Clio instrument we used for our observations has been well described elsewhere (Freed et al. (2004), Sivanandam et al. (2006), and Hinz et al. (2006)). We present only a brief overview here.

The MMT AO system delivers a lower thermal background than others because it uses the world's first deformable secondary mirror, thereby avoiding the multiple warm-mirror reflections (each adding to the thermal background) that are needed in other AO systems. This unique property makes the MMT ideal for AO observations in wavelengths such as the L' and M bands that are strongly affected by thermal glow. Clio was developed to take advantage of this to search for planets in these bands. It saw first light as a simple imager offering F/20 and F/35 modes. The design allowed for coronagrapic capability, which has since been developed (Kenworthy et al. 2007) but was not used in our survey. In the F/20 mode we used for all the observations reported herein, Clio's field of view is 15.5×12.4 arcseconds. Its plate scale is 0.04857 ± 0.00003 arcseconds per pixel, which gives finer than Nyquist sampling of the diffraction-limited point spread function (PSF) of the MMT in the L' and M bands.

Table 2—Continued

Star	RA	DEC	V	H	K	L'
GJ 3876	14:50:20.40	82:30:43.00	5.64	4.19	3.92	3.87
ξ Boo A	14:51:23.40	19:06:01.70	4.55	2.82	2.75	2.70
ξ Boo B	14:51:23.40	19:06:01.70	6.97	4.45	4.34	4.24
HD 139813	15:29:23.60	80:27:01.00	7.31	5.56	5.46	5.41
GJ 625	16:25:24.60	54:18:14.80	10.40	6.06	5.83	5.60
GJ 659 A	17:10:10.50	54:29:39.80	8.80	6.23	6.12	5.97
GJ 659 B	17:10:12.40	54:29:24.50	9.29	6.13	5.97	5.83
GJ 684 A	17:34:59.59	61:52:28.39	5.23	3.89	3.74	···
GJ 684 B	17:34:59.59	61:52:28.39	8.06	···	···	···
GJ 702 A	18:05:27.30	02:30:00.40	4.20	2.32	2.24	2.18
GJ 702 B	18:05:27.30	02:30:00.40	6.00	3.48	3.37	3.27
61 Cyg A	21:06:53.90	38:44:57.90	5.21	2.47	2.36	2.25
61 Cyg B	21:06:55.30	38:44:31.40	6.03	3.02	2.87	2.74
BD+48 3686	22:20:07.00	49:30:11.80	8.57	6.58	6.51	6.45
GJ 860 A	22:27:59.47	57:41:45.15	9.59	5.04	4.78	···
GJ 860 B	22:27:59.47	57:41:45.15	10.30	···	···	···
GJ 879	22:56:24.10	-31:33:56.00	6.48	3.80	3.81	3.70
HD 220140 A	23:19:26.60	79:00:12.70	7.54	5.74	5.66	5.60
HD 220140 B	23:19:26.60	79:00:12.70	···	···	···	···
GJ 896 A	23:31:52.20	19:56:14.10	9.95	5.24	4.99	4.64
GJ 896 B	23:31:52.20	19:56:14.10	12.40	6.98	6.68	6.28

Note. — Coordinates are epoch J2000.0 and are mostly from Perryman et al. (1997). H and K magnitudes are from Cutri et al. (2003), or else calculated from Simbad website spectral types and V magnitudes using Table 7.6 of Cox (2000). L' magnitudes are similarly calculated from either V or K values.

3.2. Observations

For each star in our sample we sought to acquire about one hour or more of cumulative integration at the L' band. In most cases we achieved this. For some of our brightest nearby targets we acquired M band integrations as well. If possible we observed the star through transit, not only to minimize airmass, but also to obtain the greatest possible amount of parallactic rotation. Parallactic rotation is important because it causes image artifacts from the telescope to rotate with respect to real sources, rendering them more distinguishable. To enhance this effect, we observed with the instrument rotator off, so that rays and ghosts from the Clio instrument itself would also rotate, and could be supressed by the same procedures that supressed telescope artifacts (see Section 3.3).

After acquiring each target with MMTAO, we determined a long 'science' exposure time based solely on the sky background, chosen so that the sky background flux filled $60-80\%$ of the detector full-well capacity. This ensured that beyond the speckle halo of the star the observations were background-limited rather than readnoise limited. Optimal exposures changed with to night-to-night variations in sky brightness; see Table 3. In normal operation Clio coadds several individual frames and saves them as a single FITS image. We used this option except for our observations of the star GJ 380, for which we saved and processed the frames individually. The increased data volume and processing runtimes for GJ 380 outweighed any minor advantages the single-frame approach may offer in terms of image quality. Coadding delivers good-quality data much more efficiently.

Table 3 shows the date on which each of our target stars was observed, the nominal single-frame integration time, the coadds, and the number of coadded FITS images we acquired. The true single-frame integration for Clio is the nominal integration plus about 59.6 msec. Table 4 gives the full science integration, parallactic rotation, and mean airmass for each star. Stellar images in our science exposures were saturated, so whenever possible we took a few shorter exposures to measure the point spread function (PSF) for each data set.

We took our data using the standard IR imaging technique of nodding, in which a sequence of images is taken in one position, the telescopes is moved ('nodded') slightly, and then another image sequence is acquired. Images taken at one position can then be subtracted from images taken at the other position. Any real celestial objects leave both bright and dark images, but artifacts of the bright sky interacting with the telescope and the detector vanish. This is a powerful technique and is practically indispensible for L' and M band observations. We typically nodded the telescope every 2-5 minutes. This was short enough that alterations in the sky background did not introduce appreciable noise into our data – in sharp contrast to, e.g., 10 μm N band observations, where a 'chopping' mirror must be used to switch between source and sky on a timescale of seconds or less.

Table 3. Observations of Science Targets: Basic Parameters

Star	Date Obs. dd/mm/yy)	Band	Clio int(msec)	Coadds	# Images
GJ 659A	11/04/06	L'	2000	10	90
GJ 354.1A	12/04/06	L'	2000	10	232
GJ 450	12/04/06	L'	2000	10	260
GJ 625	12/04/06	L'	2000	10	208
GJ 349	13/04/06	L'	2000	10	240
GJ 564	13/04/06	L'	2000	10	193
GJ 3876	13/04/06	L'	2000	25	68
GJ 3860	09/06/06	L'	1500	15	170
HD 139813	09/06/06	L'	1200	20	148
GJ 702 AB[a]	09/06/06	L'	1200	20	95
61 Cyg A	09/06/06	L'	1200	20	133
BD+60 1417	10/06/06	L'	1200	20	160
ξ Boo AB[a]	10/06/06	L'	1200	20	157
61 Cyg B	10/06/06	L'	1500	15	140
GJ 519	10/06/06	L'	1500	15	180
BD+48 3686	11/06/06	L'	1200	20	130
ξ Boo AB[a]	11/06/06	M	100	100	260
GJ 684 AB[a]	11/06/06	L'	1200	20	120
GJ 505 AB[a]	12/06/06	L'	1200	20	149
GJ 659 B	12/06/06	L'	1200	20	170
61 Cyg A	12/06/06	M	100	100	176
GJ 860 AB[a]	12/06/06	L'	1200	20	104
61 Cyg B	12/07/06	M	100	100	274
GJ 896 AB[a]	13/07/06	L'	1500	20	105
ϵ Eri	09/09/06	M	130	100	180
GJ 5	11/09/06	L'	1500	15	210
ϵ Eri	11/09/06	L'	1500	15	184
GJ 117	01/12/06	L'	1500	15	139
GJ 211	01/12/06	L'	1500	15	170
GJ 282 A	01/12/06	L'	1500	15	190
HD 1405	02/12/06	L'	1500	15	98
GJ 159	02/12/06	L'	1500	15	180

Table 3—Continued

Star	Date Obs. dd/mm/yy)	Band	Clio int(msec)	Coadds	# Images
GJ 216 A	02/12/06	L'	1500	15	158
GJ 278 C	02/12/06	L'	1500	15	132
GJ 355	02/12/06	L'	1500	15	159
GJ 879	03/12/06	L'	1500	15	54
HD 220140 AB[a]	03/12/06	L'	1500	15	170
GJ 166 BC[a]	03/12/06	L'	1500	15	149
GJ 311	03/12/06	L'	1500	15	90
GJ 410	03/12/06	L'	1500	15	100
τ Ceti	04/01/07	L'	1700	15	160
HD 29391	04/01/07	L'	1700	15	200
BD+20 1790	04/01/07	L'	1700	15	188
HD 96064 AB[a]	04/01/07	L'	1700	15	180
HD 77407 AB[a]	05/01/07	L'	1700	15	79
HD 78141[b]	11/04/07	L'	1700	15	203
HD 113449	11/04/07	L'	1500	15	190
GJ 702 AB[a]	11/04/07	M	200	100	144
GJ 380	30/04/07	L'	1500	1	2066

Note. — The 'Clio int' column gives the nominal single-frame integration time for Clio in msec. The actual single frame integration is about 59.6 msec longer in every case.

[a]These stars were sufficiently close binaries that both stars appeared on the same Clio images, and meaningful sensitivity to substellar objects could be obtained around both.

[b]A small fraction of the images of this star were accidentally taken with a 1500 msec rather than a 1700 msec nominal integration time.

Table 4. Observations of Science Targets: Data Acquired

Star	Band	Exposure(sec)	Mean Airmass	Rotation
GJ 659 A	L'	1853.64	1.113	15.80°
GJ 354.1 A	L'	4778.27	1.032	130.75°
GJ 450	L'	5354.96	1.031	110.37°
GJ 625	L'	4283.97	1.117	45.65°
GJ 349	L'	4943.04	1.178	40.61°
GJ 564	L'	3975.03	1.036	70.70°
GJ 3876	L'	3501.32	1.601	27.23°
GJ3860	L'	3976.98	1.086	47.09°
HD139813	L'	3728.42	1.529	30.15°
GJ 702 AB[a]	L'	2393.24	1.149	25.50°
61 Cyg A	L'	3350.54	1.012	101.25°
BD+60 1417	L'	4030.72	1.153	37.65°
ξ Boo AB[a]	L'	3955.14	1.047	71.20°
61 Cyg B	L'	3275.16	1.012	103.68°
GJ 519	L'	4210.92	1.011	139.97°
BD+48 3686	L'	3274.96	1.074	35.97°
ξ Boo AB[a]	M	4149.60	1.060	46.142°
GJ 684 AB[a]	L'	3023.04	1.175	24.15°
GJ 505 AB[a]	L'	3753.61	1.070	45.30°
GJ 659 B	L'	4282.64	1.112	43.93°
61 Cyg A	M	2808.96	1.025	44.24°
GJ 860 AB[a]	L'	2619.97	1.133	24.55°
61 Cyg B	M	4373.04	1.018	118.96°
GJ 896 AB[a]	L'	3275.16	1.026	66.49°
ϵ Eri	M	3412.80	1.334	23.406°
GJ 5	L'	4912.74	1.011	146.98°
ϵ Eri	L'	4304.50	1.342	36.92°
GJ 117	L'	3251.77	1.463	34.05°
GJ 211	L'	3976.98	1.097	50.12°
GJ 282 A	L'	4444.86	1.281	30.28°
HD 1405[b]	L'	2292.61	1.036	162.97°
GJ 159	L'	4210.92	1.189	37.65°
GJ 216 A	L'	3696.25	1.739	30.10°

3.3. Image Processing

Image processing for planet search AO images tends to be complex and sophisticated. We have given a brief outline of our processing pipeline in Heinze et al. (2008), which is applicable to the current work, and we hope to detail the unique aspects of our pipeline in a separate future paper. Here we will briefly describe the processing sequence, stressing aspects that were not covered in Heinze et al. (2008), but which become more important for the larger set of stars, processed over a longer period of time, that we describe herein.

We begin the processing of each Clio image by normalizing it to a single coadd, subtracting an equal-exposure dark frame usually taken immediately before or after the science data sequence, and dividing by a flat frame. There follows an initial step of bad-pixel fixing. The next step is nod subtraction: each image has subtracted from it an identically processed copy of an image from the opposite nod position. This image is scaled (by a factor that is always very close to unity) so that its mean sky brightness exactly matches that of the first image; the scaling is useful to compensate for small variations in sky brightness. Further bad-pixel fixing and bad-column correction follows. Finally, an algorithm to remove residual pattern noise is applied, and the image is zero-padded, shifted, and rotated in a single bicubic spine operation so that celestial north is up and the centroid of the primary star image is located in the exact center of the image. See Figure 1 for an example of our processing sequence, applied to the nearby binary star GJ 896.

The rotation places celestial north up on the images with an accuracy of about 0.2 degrees. Since we do not use the instrument rotator, a different rotation is required for each image: the parallactic angle plus an constant offset, which we determine by observing known binary stars. We have confirmed that the clean, symmetrical stellar images produced by the MMT AO system at the L' and M bands give accurate, consistent centroids even if saturated. While parallactic rotation of bright binary stars over just tens of seconds has been detected due to the high internal precision of Clio astrometry, in no case does sufficient parallactic rotation occur during a Clio coadd sequence to appreciably blur the science images.

We stack our processed images to make a master image for each processing method using a creeping mean combine. This method of image stacking uses a single parameter, the rejection fraction, which we set to 20% for our standard master images. The mean of each given pixel through the image stack is computed, the most deviant value is rejected, and the mean is computed again. This procedure is iterated until the required fraction of data points have been rejected. S. Sivanandam greatly improved the speed of our processing pipeline by demonstrating that the creeping mean could be computed in $N \log(N)$ time, rather than the previous N^2 implementation of A. N. H. We chose the creeping mean over the more commonly used median with sigma-clipping because the creeping mean can deliver cleaner final stacks when, as with Clio, the raw images contain bright, slowly-rotating ghosts and diffraction rays. In clean sky away from all ghosts and rays, the median delivers slightly lower rms noise, since it rejects fewer data points.

Our final stacked images contain dark, high-noise regions on either side of each bright star, due

Table 4—Continued

Star	Band	Exposure(sec)	Mean Airmass	Rotation
GJ 278 C[b]	L'	3088.01	1.017	170.627°
GJ 355	L'	3719.65	1.380	25.74°
GJ 879	L'	1263.28	2.232	11.68°
HD 220140 AB[a]	L'	3976.98	1.494	14.14°
GJ 166 BC[a]	L'	3485.71	1.301	28.66°
GJ 311	L'	2105.46	1.201	26.23°
GJ 410	L'	2339.40	1.026	34.26°
τ Ceti	L'	4223.04	1.535	37.03°
HD 29391	L'	5278.80	1.227	39.63°
BD+20 1790	L'	4962.07	1.068	47.94°
HD 96064 AB[a]	L'	4750.92	1.252	41.74°
HD 77407 AB[a]	L'	2085.13	1.008	95.44°
HD 78141[c]	L'	5297.98	1.022	109.11°
HD 113449	L'	4444.86	1.263	35.36°
GJ 702 AB	M	3738.24	1.171	32.70°
GJ 380	L'	3222.13	1.341	20.58°

[a]These stars were sufficiently close binaries that both stars appeared on the same Clio images, and meaningful sensitivity to substellar objects could be obtained around both.

[b]Though the rotation on this star is very large, difficulties arise because the star transited very near the zenith and almost all the rotation happened in a short span of time during which observations were not possible. PSF subtraction had to be performed on a subset of the data with equal numbers of images on each side of transit.

[c]A small fraction of the images of this star were accidentally taken with a 1500 msec rather than a 1700 msec nominal integration time. The total exposure time has been corrected accordingly.

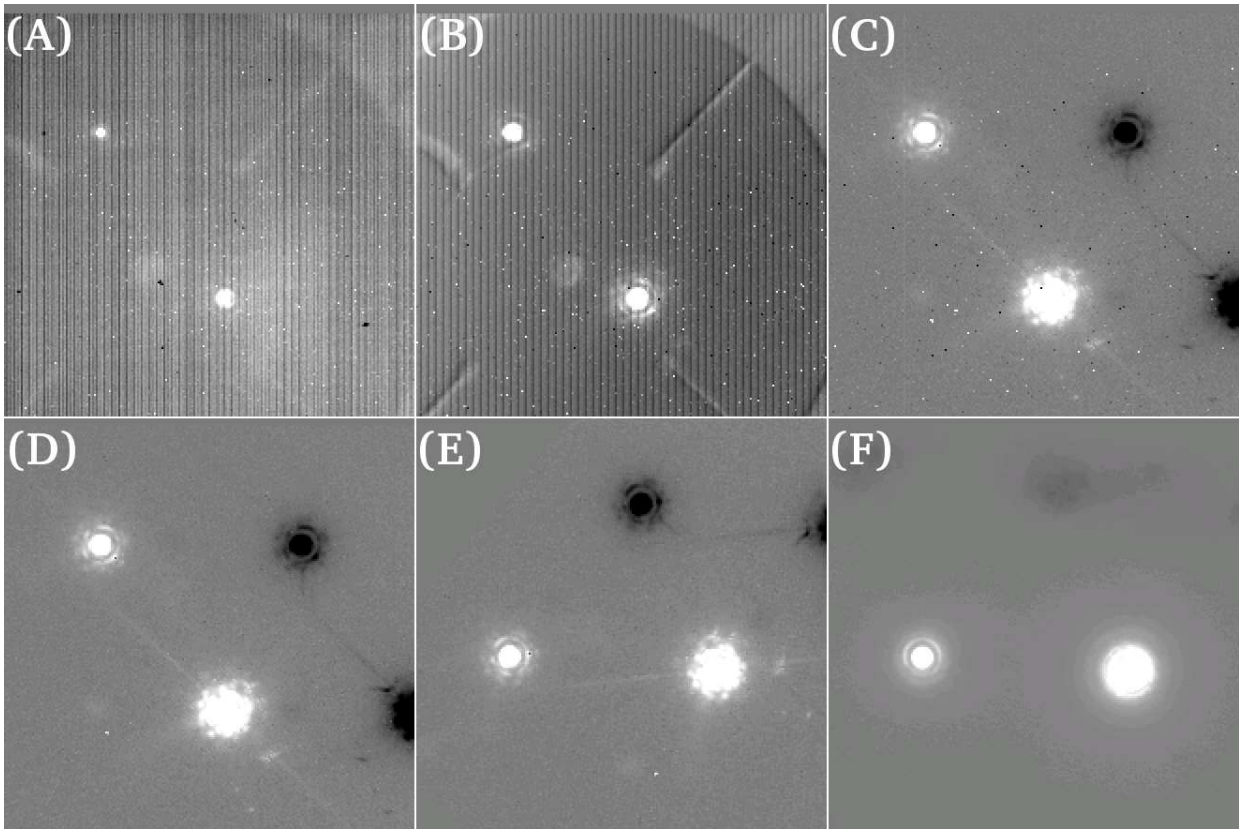

Fig. 1.— **(A)** Raw image of the nearby binary star GJ 896. **(B)** Same image after dark subtraction and flatfielding. Contrast stretched 5× relative to (A). **(C)** Same image after nod subtraction. Contrast stretched 2.5× relative to (B). **(D)** Same image after correction for bad pixels and bad columns. **(E)** Same image after shifting and rotation. **(F)** Final stack maded from 105 images like (E). Unsharp masking has not yet been applied. The field of view for each tile is 10.6 asec square.

to the negative star images from nod subtraction. Since we usually keep a constant nod direction referenced to the telescope, for data sets with significant parallactic rotation the dark regions are spread into arcs and weakened by the creeping mean stack. To further alleviate the dark regions and to enhance the visibility of faint point sources against the bright stellar halo itself, we unsharp mask the final, stacked images. We do this by convolving the image with a Gaussian kernal of $\sigma = 5$pix, and then subtracting this convolved version from the original image. The full width at half maximum (FWHM) of the Gaussian kernal is 11.8 pixels, as opposed to a FWHM of about 3 pixels for a typical PSF, so the unsharp masking does not strongly reduce the brightness of real point sources. This step marks the end of our image processing pipeline.

The above describes our baseline processing method. There were five important specializations of this method, which we called the 'b,' 'd,' 'e,' 'x,' and 'y' processing strategies, with the baseline method itself called 'a'.

In the 'b' processing method, we supress the stellar PSF to increase our sensitivity to faint companions. To do this, we take advantage of the fact that long-lived PSF artifacts in stellar images from AO-equipped telescopes tend to remain fixed with respect to the telescope and/or instrument. When observing with the instrument-rotator off, as we do, real sources slowly rotate with respect to artifacts as the telescope tracks. Science images must be digitally rotated before stacking, as described above. However, if a stack of *un*-rotated frames is made, a clear image of the instrumental PSF is obtained, while any real sources are strongly attenuated by the creeping mean. We subtract a properly registered version of such a PSF image from every science frame prior to final rotation and stacking. The result is powerful attenuation of the stellar PSF and greatly increased sensitivity to close-in companions. Marois et al. (2006) appear to have been the first to use a procedure like this for AO planet imaging; they describe it as angular differential imaging (ADI).

In the 'd' reduction method, each image is unsharp masked *before* the stack. The final stacked image is unsharp masked again. This method improves every data set, and is especially powerful for bright stars whose intense seeing halos tend to introduce noise into the final stacks. The 'e' data reduction method combines the 'b' and 'd' methods: ADI is applied, and then the pre-stack unsharp masking is performed.

The 'x' data reduction method uses a variant on nod subtraction that avoids the dark negative images. Two master sky images are made, by combining the star-free portions of all images in the first and second halves of the data set. One of these star-free master sky images is then subtracted from each individual science image in lieu of the ordinary nod subtraction. To avoid subtracting real sources, the sky image from the second half of the data set is subtracted from images in the first half, and vice-versa. The usefulness of this processing method varies enormously from one data set to another. If the sky background was very stable, the dark nod-subtraction artifacts disappear magically, and the background noise level is almost as good as for the baseline processing. If the sky background was highly variable, the 'x' images are useless due to intense noise. The 'y' image reduction method is a combination of the 'x' and 'd' methods, in which the images are unsharp

masked after the subtraction of the master sky image but before the final stack. Figure 2 compares the results of the 'a' method (before and after the final unsharp masking step), the 'd' method, and the 'y' method. The star is HD 96064, a binary system in which the secondary is itself a close binary. A faint additional companion is also detected, but is confirmed based on $K_S - L'$ color to be a background star rather than a substellar companion.

Two additional processing methods could be applied to binary stars of near-equal brightness in which both components appeared on each Clio frame. A scaled version of the PSF of each star could be used to subtract the other, on a frame-by-frame basis, prior to the final stack. The resulting PSF subtraction was substantially better than ADI. We labeled this reduction method 'f.' A version that also included pre-stack unsharp masking was called 'g'. Figure 3 illustrates our different PSF subtraction methods, both ADI and binary star subtraction, as applied to the binary star GJ 896, which was also shown in Figure 1.

We applied the 'a,' 'b,' 'd,' and 'e' processing methods to almost all of our stellar data sets, except a very few for which there was insufficient parallactic rotation to use the ADI methods without subtracting real sources. In many instances we also applied the 'x' and 'y' methods. We applied the 'f' and 'g' methods to every binary star where they would work.

The methods involving pre-stack unsharp masking ('d,' 'e,' 'y,' and 'g') always gave cleaner images, but we used the other methods as well because pre-stack masking slightly dimmed point sources (by about 3-10%, depending on the AO-corrected FWHM), and there was a slight chance this could cause a discovery to be missed. Our pattern-noise correction method also dimmed faint point sources by about 15-18%, based on tests. Near the end of our processing, we implemented a superior pattern-noise correction originated by M. K. that caused zero dimming, and a new form of unsharp masking which also produced zero dimming to within the measurement error of our tests. Only the stars GJ 684 A, GJ 684 B, GJ 702 A (M band only), GJ 702 B (M band only), 61 Cyg B (M band only), GJ 860 A, and GJ 860 B were processed using these improvements. For these stars, only the 'd,' 'e,' 'y,' and, where applicable, the 'g' processing methods were used, since the downside of pre-stack unsharp masking had been eliminated.

4. Sensitivity Analysis

4.1. Sensitivity Estimators

Our survey arrived at a null result: no planets were detected. Our science results, like those of previous surveys (Masciadri et al. 2005; Kasper et al. 2007; Biller et al. 2007; Lafrenière et al. 2007), therefore take the form of upper limits on the abundance of extrasolar planets. The accuracy of such an upper limit depends entirely on having a good metric for the sensitivity of the survey observations.

A sensitivity estimator must translate some measurable statistic of an image into a realistic

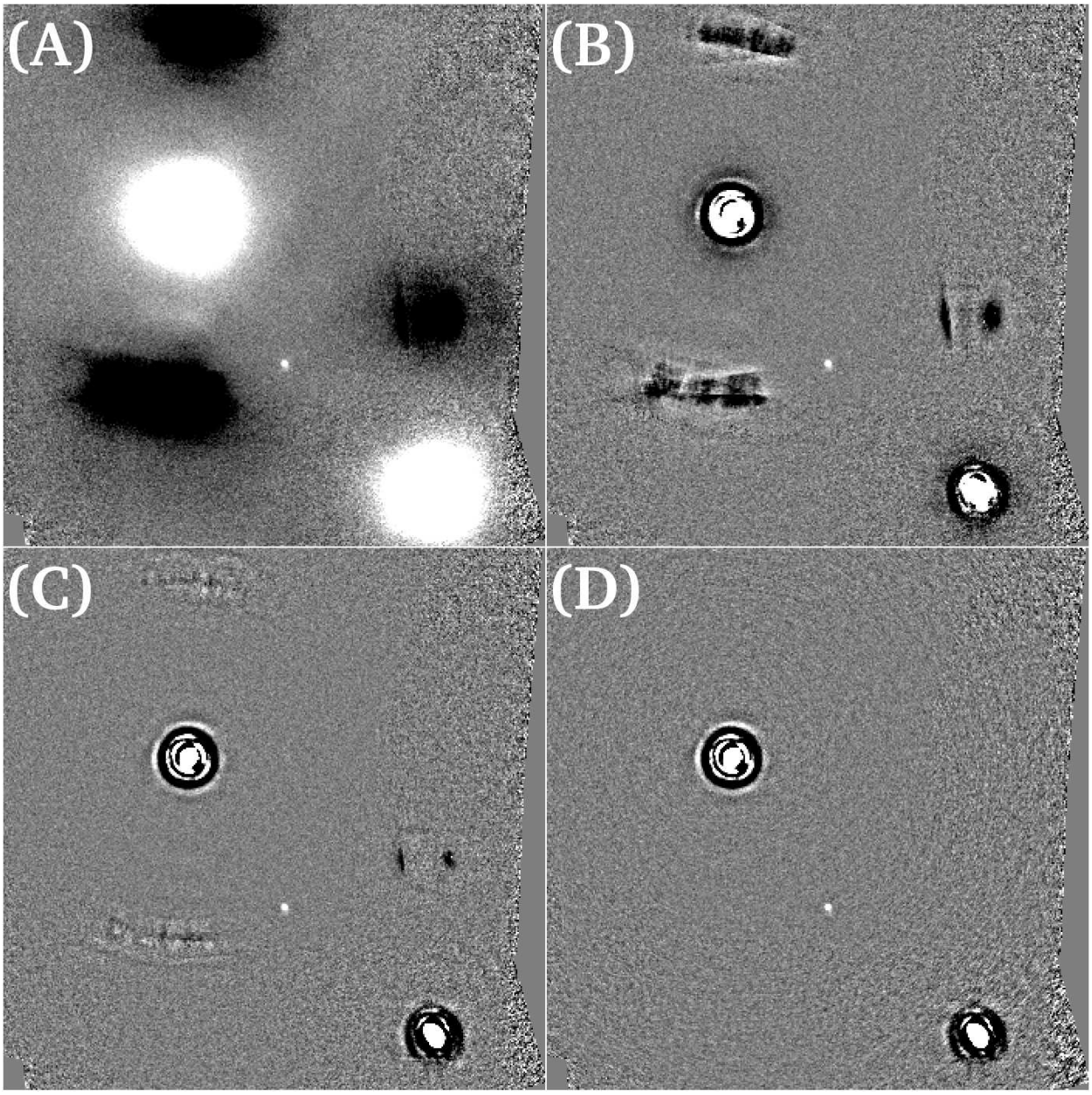

Fig. 2.— **(A)** Result of baseline processing ('a' method) before final unsharp mask. **(B)** The 'a' method image after unsharp masking. Dark nod-subtraction artifacts are somewhat reduced but remain prominent. **(C)** Same data set processed with the 'd' method. Nod artifacts are greatly reduced, but still exist as high-noise regions where faint sources could not be detected. **(D)** Same data set processed with the 'y' method. The nod artifacts are eliminated. Field shown in each tile is 17 asec square.

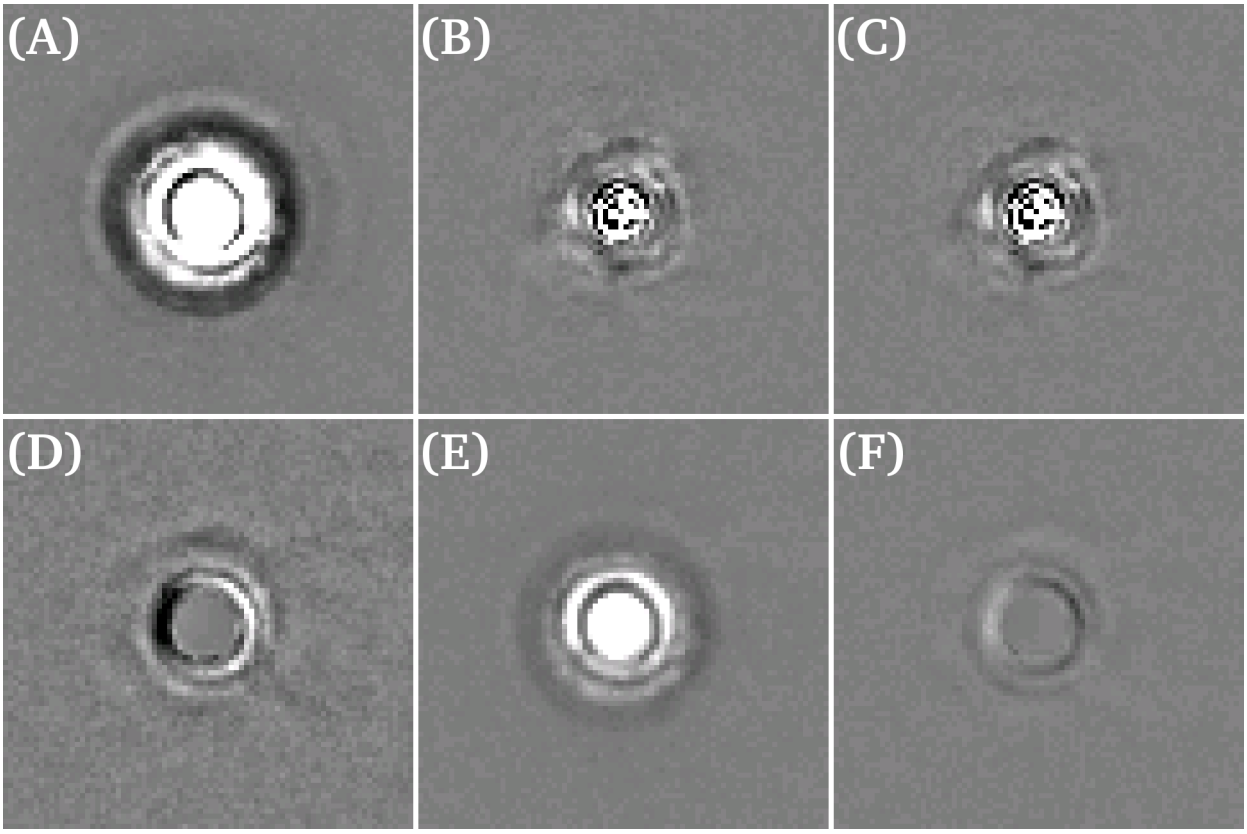

Fig. 3.— **(A)** Baseline 'a' method final image of GJ 896A. **(B)** Same data set processed with ADI ('b' method). **(C)** Same data set processed with ADI and pre-stack unsharp masking ('e' method). **(D)** Same data set processed with binary star subtraction. Background noise is increased because the secondary had to be scaled up to match the brightness of the primary. **(E)** Same data set, but now showing the 'a' method image of the secondary, rather than the primary. **(F)** Same data set, again showing the secondary, but now processed with binary star subtraction. The background is very clean since the primary was scaled down to subtract away the secondary. Field shown in each tile is 3.9 asec square.

point-source detection limit. For well-sampled data such as ours, perhaps the simplest solution is to calculate the RMS of pixel values in an assigned region and translate this to a detection limit using simple $\sqrt{n}$ statistics:

$$\sigma_{PSF} = \sigma_{pix}\sqrt{\pi r^2} = \sigma_{pix} r \sqrt{\pi}. \quad (1)$$

Where σ_{PSF} is the PSF-scale noise in the image, σ_{pix} is the sigle-pixel rms, and r is the radius of the image of a point source (i.e. about half the FWHM of the PSF). Since not all the flux of a real point source will fall within the aperture of radius r, an aperture correction must be applied as a final step. Then, for example, the 5σ point-source sensitivity will be 5 σ_{PSF} times the aperture correction. We will call this Method 1.

The simple $\sqrt{n}$ statistics used in Method 1 assume that the brightness of each pixel is a random variable independent of its neighboring pixels: that is, that the noise is spatially uncorrelated. This assumtion is violated for speckle residuals close to a star, and for a host of other stellar artifacts that are present in AO images (ghosts, diffraction rays, etc.). We have confirmed by careful tests that in the presence of speckle noise, Method 1 overestimates the true point-source sensitivity by up to 0.9 magnitudes. This applies to a good implementation of the method in which σ_{pix} is calculated over image regions spanning many PSF sizes. When the statistics region used is too small, the sensitivity will be overestimated even more.

The problem with Method 1 is that clumps of correlated bright or dark pixels introduce more PSF-scale noise into the image than can be predicted from the single-pixel RMS. A simple solution is to sums up the brightness within many apertures of radius r, spaced through an assigned region, and then σ_{PSF} is simply the RMS variation of the sums. This is sensitivity estimation by aperture photometry of the noise background. Again, it is important to calculate the statistic over an image region large enough to contain many PSFs. We will call this Method 2. As with Method 1, an aperture correction must be applied as a final step.

Method 3 has already been described in Heinze et al. (2008). It is analagous to Method 2, but rather than performing aperture photometry at many locations in the image, one performs PSF-fitting photometry. If the PSF has been properly normalized, no aperture correction is necessary for this method. In tests using our own real data, we find that Methods 2 and 3 agree to within reasonable uncertainty everywhere, while Method 1 agrees with the other two only in regions of very clean sky. Method 1 overestimates the sensitivity by about 0.2 magnitudes in the presence even of very faint ghost residuals, and by about 0.9 magnitudes in the strong residual speckle noise close to the star. In a field where Method 1-like estimators have been widely used, this should constitute a warning: they severely overestimate sensitivity at small angular separations from stars, where planets are probably most likely to occur!

Herein, as in Heinze et al. (2008), we have used Method 3 for our final sensitivity maps. Far from the primary star star, the region we use for calculating the sensitivity statistic is a disk of

radius 8 pixels (0.39 arcsec, or about 3 λ/D): that is, large enough to span many PSF-sizes, but small enough to sample the local noise properties. Close to the star (that is, within 60 pixels or 2.9 arcsec), we use instead an arc 45 pixels (2.2 arcsec) long and 1 pixel wide, at a fixed radius from the star. These disks or arcs are centered in turn on every pixel of each image, with the calculated statistics forming a sensitivity map.

4.2. Sensitivity Obtained

After making a sensitivity map from the stacked image produced by each processing method applied to the data from a given star, we apply a slight smoothing to the different maps, and then combine them into a single master sensitivity map. They are combined such that the master sensitivity image shows at each location the best sensitivity obtained at that location by any processing method that was applied. We quote 10σ sensitivities: that is, the point source sensitivity is ten times the σ_{PSF} statistic from Method 3. Figures 4, 5, and 6 give example sensitivity contour maps for our L' observations of GJ 896 and GJ 117, and our M band observations of 61 Cyg B, respectively, with 10σ sensitivities given in apparent magnitudes. Figures of this type for all the stars observed in our survey can be downloaded from http://www.hopewriter.com/Data/SurveyPaper/.

For use in the Monte Carlo simulations to be described in Section 7 below, we have converted our sensitivity maps into plots of sensitivity vs. projected radius from each star. As can be seen from Figures 4 through 6, however, our sensitivity varied widely with position angle around the star. To quantify this, we calculated ten different sensitivity values at each radius, giving the percentiles in sensitivity from 0th to 90th percentile in 10% increments. Thus, e.g., the 0th percentile at 2 asec is the very worst sensitivity obtained anywhere on the 2 asec-radius ring surrounding the star, while the 50th percentile gives the median sensitivity at that radius. In Figures 7 and 8, we give example plots for GJ 896 A, GJ 117, 61 Cyg B (M band), and ϵ Eri, with the sensitivities converted to minimum detectable planet mass in MJ using models from Burrows et al. (2003), plotted against projected separation in AU. Plots of this type for all the stars in our survey, as well as the tabular data from which they were constructed, can be downloaded from http://www.hopewriter.com/Data/SurveyPaper/.

4.3. Source Detection

While our final sensitivity maps are constructed using only Method 3, as described above, we use both Methods 2 and 3 for automated source detection. The use of both methods increases our likelihood of noticing faint sources at the limit of detectability. To search an image for sources using either method, we query each pixel in turn to see if a source is present at that location. First, we calculate the sensitivity statistic (Method 2 or Method 3) over either a disk or an arc, just as described in Section 4.1, except that a PSF-sized region around the pixel being considered is not

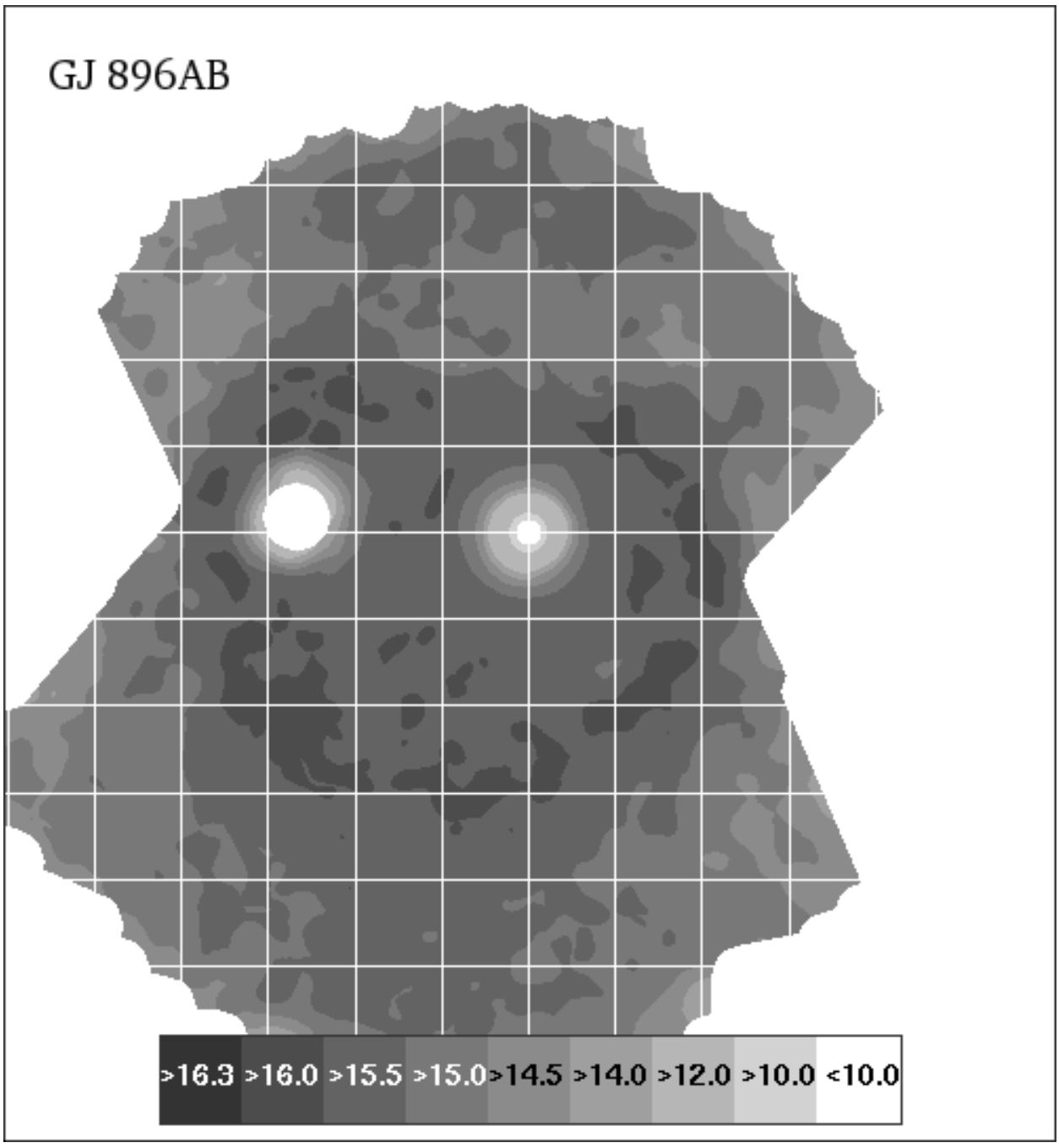

Fig. 4.— Final sensitivity contour map for the binary star GJ 896 AB. 10σ sensitivities from our Method 3 estimator are presented, converted to apparent L' magnitudes. The grid squares superposed for astrometric reference are 2×2 arcsec. The darkest contour from the colorbar is not present as the 10σ sensitivity in this data set never exceeded $L' = 16.3$.

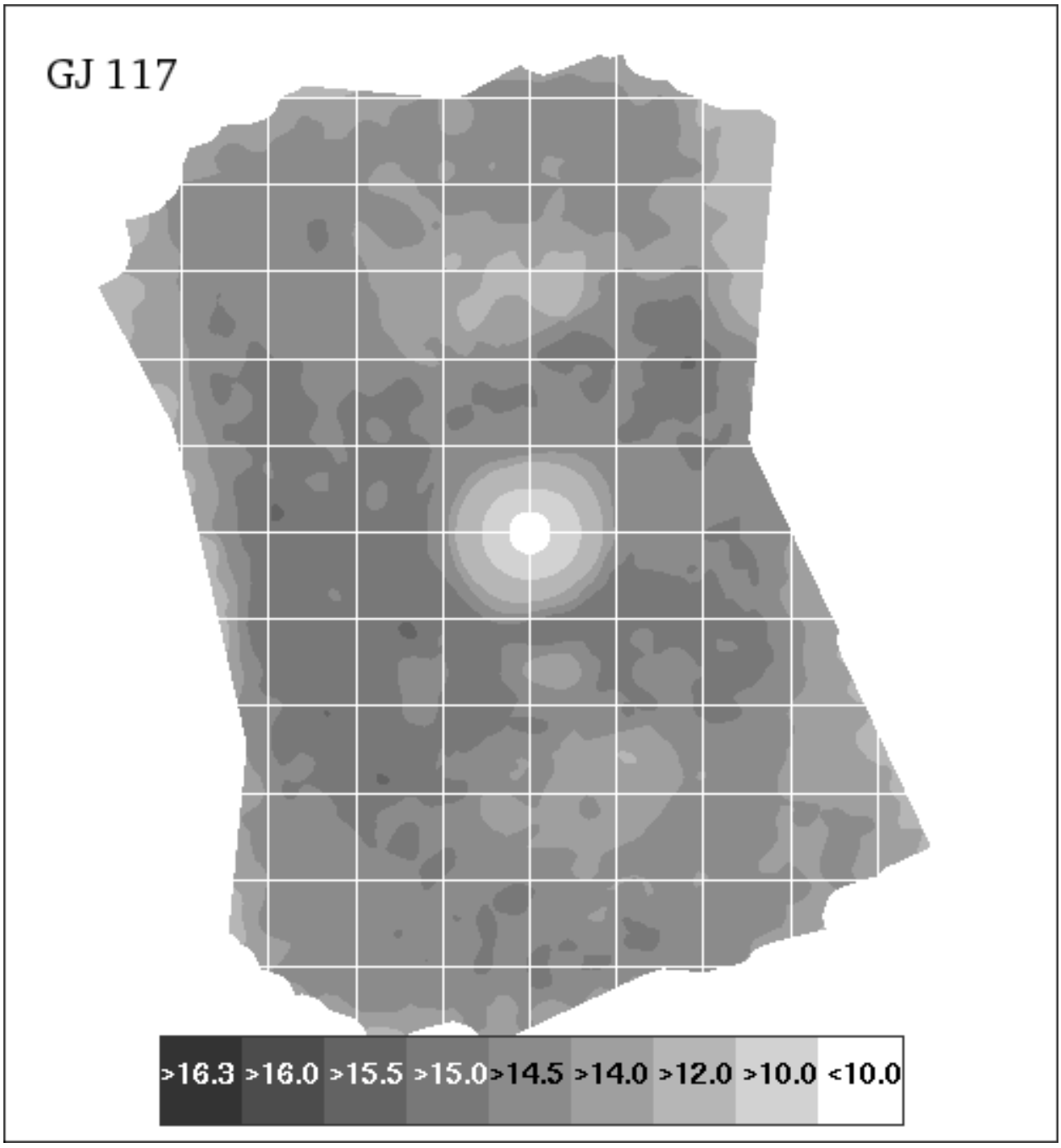

Fig. 5.— Final sensitivity contour map for the star GJ 117. 10σ sensitivities from our Method 3 estimator are presented, converted to apparent L' magnitudes. The grid squares superposed for astrometric reference are 2×2 arcsec, with the primary star in the figure's center. The darkest two contours from the colorbar are not present as the 10σ sensitivity in this data set never exceeded $L' = 16.0$.

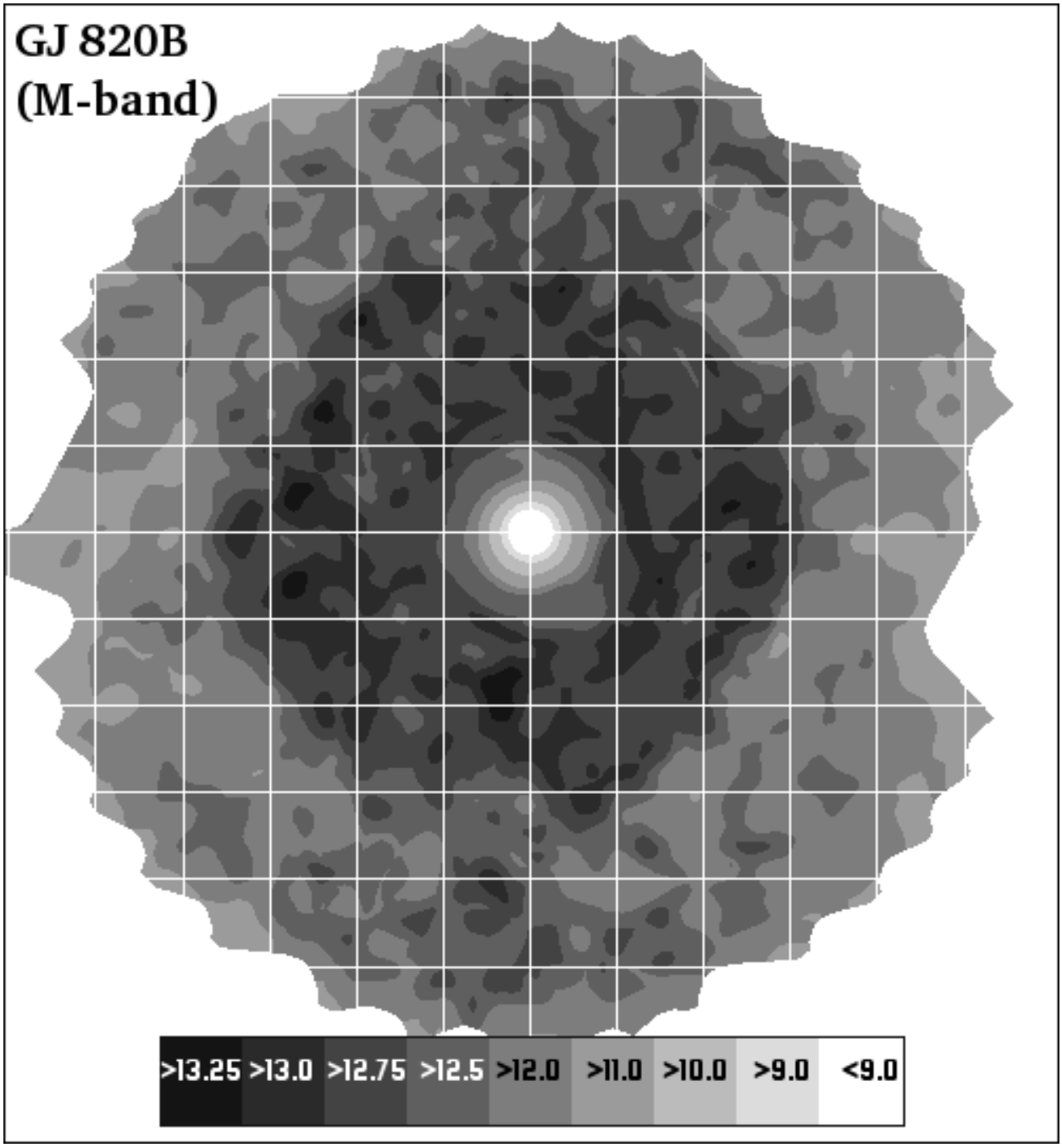

Fig. 6.— Final sensitivity contour map for our M band observations of the star 61 Cyg B (GJ 820 B). 10σ sensitivities from our Method 3 estimator are presented, converted to apparent M band magnitudes. The grid squares superposed for astrometric reference are 2×2 arcsec.

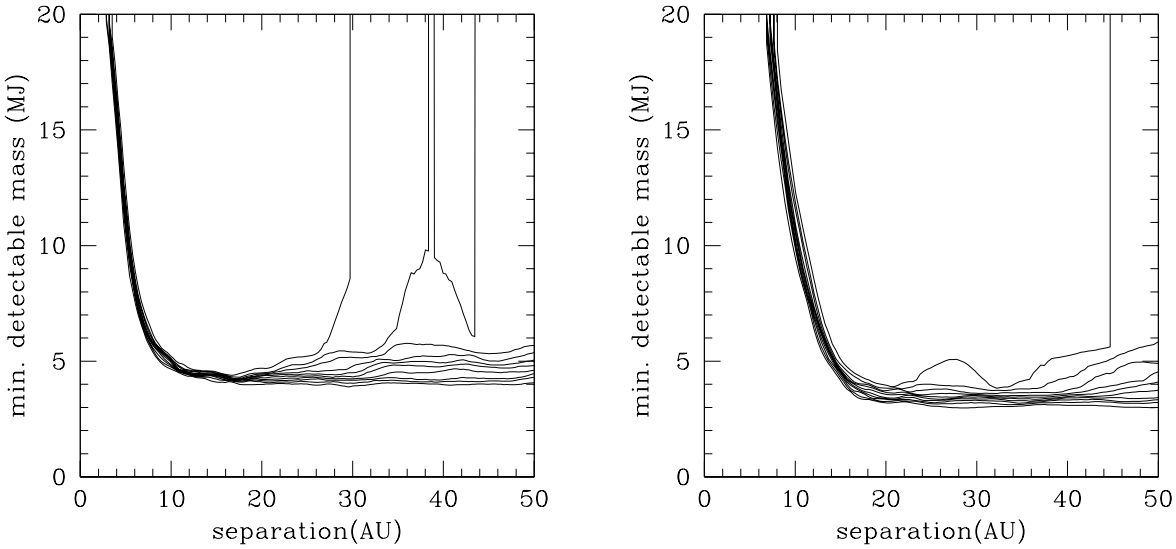

Fig. 7.— Minimum detectable planet mass vs. projected separation in AU for GJ 896 A (left) and GJ 117 (right). 10σ detection limits from Method 3 are shown, converted to planet mass using models from Burrows et al. (2003). Planetary orbits around GJ 896 A would be destabilized beyond about 12 AU by the companion star GJ 896 B. In order from bottom to top, the curves give the 90th, 80th, 70th, 60th, 50th, 40th, 30th, 20th, 10th, and 0th percentile sensitivity at each radius.

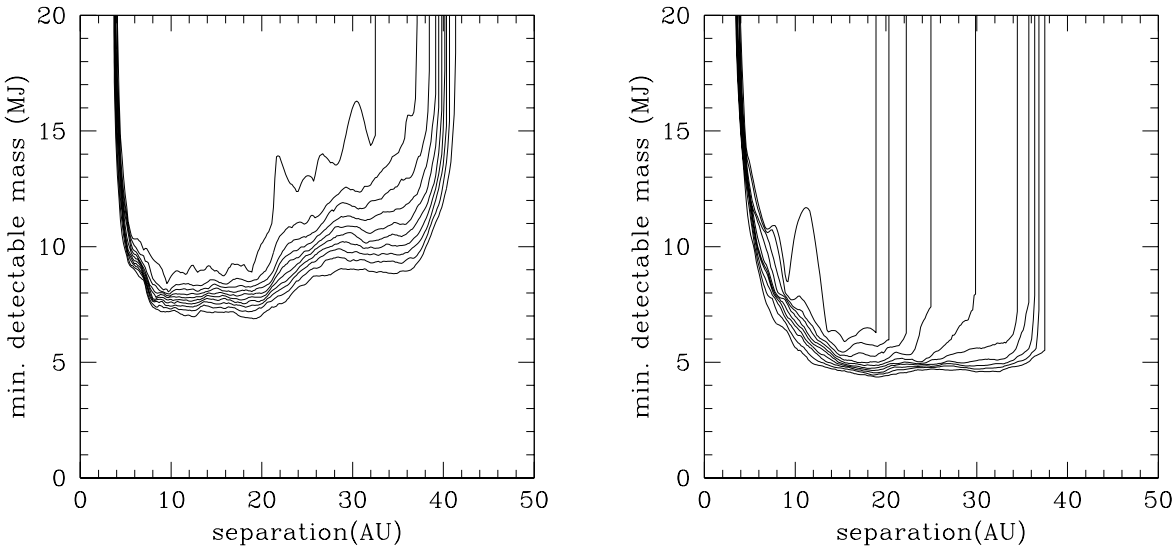

Fig. 8.— Minimum detectable planet mass vs. projected separation in AU for 61 Cyg B (M band data; left), and ϵ Eri (right). 10σ detection limits from Method 3 are shown, converted to planet mass using models from Burrows et al. (2003). In order from bottom to top, the curves give the 90th, 80th, 70th, 60th, 50th, 40th, 30th, 20th, 10th, and 0th percentile sensitivity at each radius.

included, so that if a real source is present, it will not bias the sensitivity estimator. Finally, either aperture photometry (Method 2) or PSF-fitting (Method 3) is applied at the location of the pixel itself, measuring the brightness of any source that may be present there. If the resulting brightness is greater than the sensitivity statistic by a specified threshold factor (i.e., 5 for a 5σ detection), a preliminary detection is reported.

We would like to set the threshold as low as possible without getting an unmanageable number of spurious detections. To this end, we divided each data set into the first half of the images and the second half, and created a stacked image from each half. To be reported by our automated detection code, a source had to appear at 4.5σ significance in the full stack, and at 3σ significance on each half-stack, at a location consistent to within 2 pixels. This eliminated residual ghosts and other artifacts, which would appear in different locations on the two halves of the data due to parallactic rotation. Around 10-20 spurious automated detections were nonetheless reported around each star.

A real source could also be missed by the automatic algorithm but noticed manually. For example, due to parallactic rotation, a location might have valid data only for the first half of the data sequence, rendering an automated detection of a real source there impossible. Every automated detection, as well as candidate sources noticed only by eye, was carefully examined manually. Criteria applied included correct FWHM and symmetry, consistency in position and brightness from one half-stack to the other, and inability to be explained away as an artifact of ghosts, diffraction rays, etc. If necessary, data stacks were split into quarters or even finer divisions to verify sources where only a fraction of the images provided useful data. Every source that passed this final manual analysis was found to correspond to a real astronomical object. There were no false positives.

4.4. Blind Sensitivity Tests

The final demonstration of the validity of a sensitivity estimator is a blind sensitivity test, in which fake planets are inserted into the raw data and then recovered by an experimenter (or automated process) without a-priori knowledge of their positions or their number. Such a blind test is the surest way to evaluate any sensitivity estimator and establish the relationship between nominal significance (i.e. 3σ, 5σ, etc.) and the true completeness level of the survey. This should be standard procedure for all planet imaging surveys.

We inserted simulated planets at random locations in the raw data for selected stars. The flux of each simulated planet was scaled to 5, 7, or 10σ significance based on the master sensitivity map described above. The data was then processed exactly as for the real, unmodified science data for that star, and planets were sought in the fully processed images by the same combination of manual and automatic methods used for the real images.

The final result of each test was that every inserted planet was classified as 'Confirmed', 'No-

ticed', or 'Unnoticed'. 'Confirmed' means the source was confidently detected, with no significant doubt of its being a real object. 'Noticed' means the source was flagged by our automatic detection algorithm, or noticed manually as a possible real object, but could not be confirmed beyond reasonable doubt. Many spurious sources are 'Noticed' whereas the false-positive rate for 'Confirmed' detections is extremely low, with none for any of the data sets discussed here. 'Unnoticed' means a fake planet was not automatically flagged or noticed manually.

Tables 5 through 9 give the results of these simulations.

Table 5. GJ 450 fake planet experiment.

Sep (asec)	L' Mag	Mass (MJ)	Detection Significance	Status
0.51	12.53	>20	10.00σ	Confirmed
0.56	13.32	>20	10.00σ	Confirmed
0.95	15.35	11.26	10.00σ	Confirmed
1.14	15.60	10.54	10.00σ	Confirmed
1.27	15.96	9.51	10.00σ	Confirmed
1.58	16.06	9.21	10.00σ	Confirmed
1.90	16.51	7.93	10.00σ	Confirmed
2.50	16.59	7.73	10.00σ	Confirmed
2.69	16.57	7.78	10.00σ	Confirmed
2.91	16.38	8.29	10.00σ	Confirmed
2.98	16.60	7.70	10.00σ	Confirmed
3.71	16.51	7.93	10.00σ	Confirmed
3.90	16.59	7.73	10.00σ	Confirmed
3.93	16.62	7.65	10.00σ	Confirmed
5.02	16.49	7.98	10.00σ	Confirmed
6.52	16.43	8.15	10.00σ	Confirmed
6.53	16.27	8.61	10.00σ	Confirmed

Note. — All of the input planets were confirmed. Planet magnitude to mass conversion carried out by interpolation based on theoretical spectra from Burrows et al. (2003).

Table 6. HD 29391 fake planet experiment.

Sep (asec)	L' Band Mag	Mass (MJ)	Detection Significance	Status
0.42	11.59	>20	10.00σ	Confirmed
0.76	12.56	16.85	10.00σ	Confirmed
1.23	15.35	4.97	10.00σ	Confirmed
2.06	15.90	3.92	10.00σ	Confirmed
2.27	16.10	3.63	10.00σ	Confirmed
3.26	14.58	6.95	10.00σ	Confirmed
3.60	15.77	4.15	10.00σ	Confirmed
4.29	15.48	4.72	10.00σ	Confirmed
4.41	16.22	3.46	10.00σ	Confirmed
5.31	16.21	3.47	10.00σ	Confirmed
8.92	16.15	3.56	10.00σ	Confirmed
10.69	16.15	3.56	10.00σ	Confirmed
1.25	15.17	5.40	7.00σ	Confirmed
1.86	16.32	3.31	7.00σ	Confirmed
2.00	16.47	3.09	7.00σ	Unnoticed
2.69	16.54	2.99	7.00σ	Unnoticed
2.92	16.61	2.93	7.00σ	Noticed
3.29	16.47	3.09	7.00σ	Confirmed
4.69	15.83	4.03	7.00σ	Noticed
5.72	16.38	3.22	7.00σ	Confirmed
6.28	15.97	3.82	7.00σ	Noticed
10.53	15.94	3.86	7.00σ	Confirmed
1.19	15.39	4.89	5.00σ	Confirmed
1.93	16.77	2.78	5.00σ	Noticed
5.76	16.57	2.97	5.00σ	Noticed
6.68	16.25	3.41	5.00σ	Unnoticed
7.70	16.18	3.51	5.00σ	Unnoticed

Note. — Planets confirmed: 12/12 at 10σ; 5/10 at 7σ; 1/5 at 5σ. Planets noticed: 12/12 at 10σ; 8/10 at 7σ; 3/5 at 5σ.

Planet magnitude to mass conversion carried out by interpolation based on theoretical spectra from Burrows et al. (2003).

Table 7. GJ 117 fake planet experiment.

Sep (asec)	L' Band Mag	Mass (MJ)	Detection Significance	Status
0.67	10.41	>20.0	10.00σ	Confirmed
0.94	11.54	15.42	10.00σ	Confirmed
1.10	12.05	12.21	10.00σ	Confirmed
2.11	15.01	3.42	10.00σ	Confirmed
2.17	14.78	3.75	10.00σ	Confirmed
3.31	14.93	3.53	10.00σ	Confirmed
3.77	15.20	3.14	10.00σ	Confirmed
6.40	14.72	3.84	10.00σ	Confirmed
6.42	15.26	3.05	10.00σ	Confirmed
8.60	15.06	3.35	10.00σ	Confirmed
9.88	14.56	4.09	10.00σ	Confirmed
1.14	12.54	9.77	7.00σ	Confirmed
3.08	15.44	2.87	7.00σ	Noticed
5.06	15.35	2.96	7.00σ	Confirmed
6.37	14.67	3.91	7.00σ	Noticed
7.04	14.66	3.93	7.00σ	Noticed
7.88	15.27	3.05	7.00σ	Noticed
1.04	12.31	10.83	5.00σ	Confirmed
1.75	15.12	3.26	5.00σ	Unnoticed
2.89	15.96	2.40	5.00σ	Unnoticed
3.30	16.16	2.21	5.00σ	Unnoticed
5.08	16.00	2.36	5.00σ	Confirmed
7.80	15.32	2.98	5.00σ	Noticed
8.03	15.65	2.68	5.00σ	Unnoticed
10.21	15.30	3.00	5.00σ	Noticed

Note. — Planets confirmed: 11/11 at 10σ; 2/6 at 7σ; 2/8 at 5σ. Planets noticed: 11/11 at 10σ; 6/6 at 7σ; 4/8 at 5σ. Planet magnitude to mass conversion carried out by interpolation based on theoretical spectra from Burrows et al. (2003).

Note that a fake planet with a mass of only 2.36 MJ was confirmed.

Table 8. GJ 355 fake planet experiment.

Sep (asec)	L' Band Mag	Mass (MJ)	Detection Significance	Status
0.37	9.46	>20.0	10.00σ	Confirmed
0.43	9.66	>20.0	10.00σ	Confirmed
0.94	13.72	13.10	10.00σ	Confirmed
1.67	15.61	5.74	10.00σ	Confirmed
1.74	15.66	5.63	10.00σ	Confirmed
1.85	15.74	5.43	10.00σ	Confirmed
2.05	15.63	5.70	10.00σ	Confirmed
2.37	15.87	5.11	10.00σ	Noticed
3.08	15.60	5.78	10.00σ	Confirmed
3.30	15.92	5.00	10.00σ	Confirmed
3.44	15.73	5.46	10.00σ	Confirmed
4.26	16.02	4.80	10.00σ	Confirmed
5.55	15.87	5.12	10.00σ	Confirmed
8.09	15.55	5.89	10.00σ	Confirmed
8.70	15.34	6.46	10.00σ	Confirmed
1.57	15.95	4.93	7.00σ	Noticed
2.83	16.24	4.37	7.00σ	Noticed
3.68	16.04	4.77	7.00σ	Confirmed
4.34	16.01	4.82	7.00σ	Confirmed
4.68	16.33	4.19	7.00σ	Noticed
6.99	15.95	4.94	7.00σ	Confirmed
1.92	16.58	3.78	5.00σ	Unnoticed
3.24	16.52	3.87	5.00σ	Unnoticed
5.61	15.93	4.99	5.00σ	Noticed
5.99	15.86	5.16	5.00σ	Noticed
7.17	15.94	4.97	5.00σ	Noticed
10.07	16.31	4.23	5.00σ	Confirmed

Note. — Planets confirmed: 14/15 at 10σ; 3/6 at 7σ; 1/6 at 5σ. Planets noticed: 15/15 at 10σ; 6/6 at 7σ; 4/6 at 5σ. Planet magnitude to mass conversion carried out by interpolation based on theoretical spectra from Burrows et al. (2003).

The total statistics from all 5 blind tests are that 63 of 65 planets were confirmed at 10σ, 13 of 28 at 7σ, and 4 of 25 at 5σ. In percentages we have 97% completeness at 10σ, 46% completeness at 7σ, and 16% completeness at 5σ.

Note the very low completeness at 5σ, which many past surveys have taken as a realistic detection limit. Though sensitivity estimators (and therefore the exact meaning of 5σ) differ, ours was quite conservative. The low completeness we find at 5σ should serve as a warning to future workers in this field, and an encouragement to establish a definitive significance-completeness relation through blind sensitivity tests as we have done. Many more planets were noticed than were confirmed: for noticed planets, the rates are 100% at 10σ, 86% at 7σ, and 56% at 5σ. However, very many false positives were also noticed, so sources that are merely noticed but not confirmed do not represent usable detections. No false positives were confirmed in any of our blind tests.

Our low 5σ completeness level for confirmed planets has several causes. First, some flux is lost from faint sources in our processing, as described above, so that sources input at 5σ significance are reduced to a real significance of typically 4σ in the final image. Second, since our images contain speckles, ghosts, diffraction rays, and pattern noise, the noise is not gaussian but rather has a long tail toward improbable, bright events. Third, the area of each final image is over 10^5 times the size of a PSF, so the distribution of possible spurious planet images arising from noise is sampled at least 10^5 times for each final image in our survey. Followup observations of suspected sources are costly in terms of telescope time, so a detection strategy with a low false-positive rate is important. Some or all of these considerations apply to all other planet-imaging surveys, again making blind sensitivity tests important.

5. Detections of Faint Real Objects

5.1. Overview of Detected Companions

In all, thirteen faint sources were confirmed as real. Table 5.1 presents our astrometry and photometry for each detected companion.

Of these 13 faint companions, one is a newly discovered low mass star orbiting GJ 3876, one is a previously known binary brown dwarf companion to GJ 564 (Potter et al. 2003), and the other eleven are background stars. Note that Lafrenière et al. (2007), operating in the H band regime, found more than 300 background stars. Due to the red IR colors of planets, a long wavelength survey such as ours can obtain good sensitivity to planets while remaining blind to all but the brightest stars, so that less telescope time is needed to follow up candidate objects. Also, a background star masquerading as a planet at L' can often be detected in a short integration at shorter wavelengths, showing that the object is far too blue in IR color to be a planet. We have used this method to confirm that the brighter of the two companions of BD+20 1790 and the faint companions near HD 96064, BD+60 1417, and GJ 3860 are background stars. It gives results immediately, in contrast

Table 9. BD+48 3686 fake planet experiment.

Sep (asec)	L' Band Mag	Mass (MJ)	Detection Significance	Status
0.23	8.03	>20.0	10.00σ	Confirmed
0.97	14.65	13.89	10.00σ	Noticed
1.33	15.19	10.47	10.00σ	Confirmed
2.05	15.51	9.05	10.00σ	Confirmed
4.33	15.57	8.85	10.00σ	Confirmed
5.08	15.70	8.41	10.00σ	Confirmed
6.13	15.52	9.04	10.00σ	Confirmed
6.34	14.70	13.53	10.00σ	Confirmed
8.41	15.38	9.60	10.00σ	Confirmed
9.73	15.46	9.26	10.00σ	Confirmed
1.46	15.62	8.67	7.00σ	Confirmed
2.55	15.86	7.87	7.00σ	Noticed
3.76	16.15	7.05	7.00σ	Unnoticed
5.25	15.72	8.32	7.00σ	Confirmed
5.73	15.66	8.53	7.00σ	Unnoticed
10.43	15.41	9.50	7.00σ	Confirmed
1.08	15.63	8.66	5.00σ	Noticed
3.04	16.39	6.45	5.00σ	Unnoticed
3.34	16.29	6.70	5.00σ	Unnoticed
5.69	16.40	6.42	5.00σ	Noticed
9.19	16.17	7.00	5.00σ	Unnoticed
10.22	15.97	7.56	5.00σ	Noticed

Note. — Planets confirmed: 9/10 at 10σ; 3/6 at 7σ; 0/6 at 5σ. Planets noticed: 10/10 at 10σ; 4/6 at 7σ; 3/6 at 5σ. Planet magnitude to mass conversion carried out by interpolation based on theoretical spectra from Burrows et al. (2003).

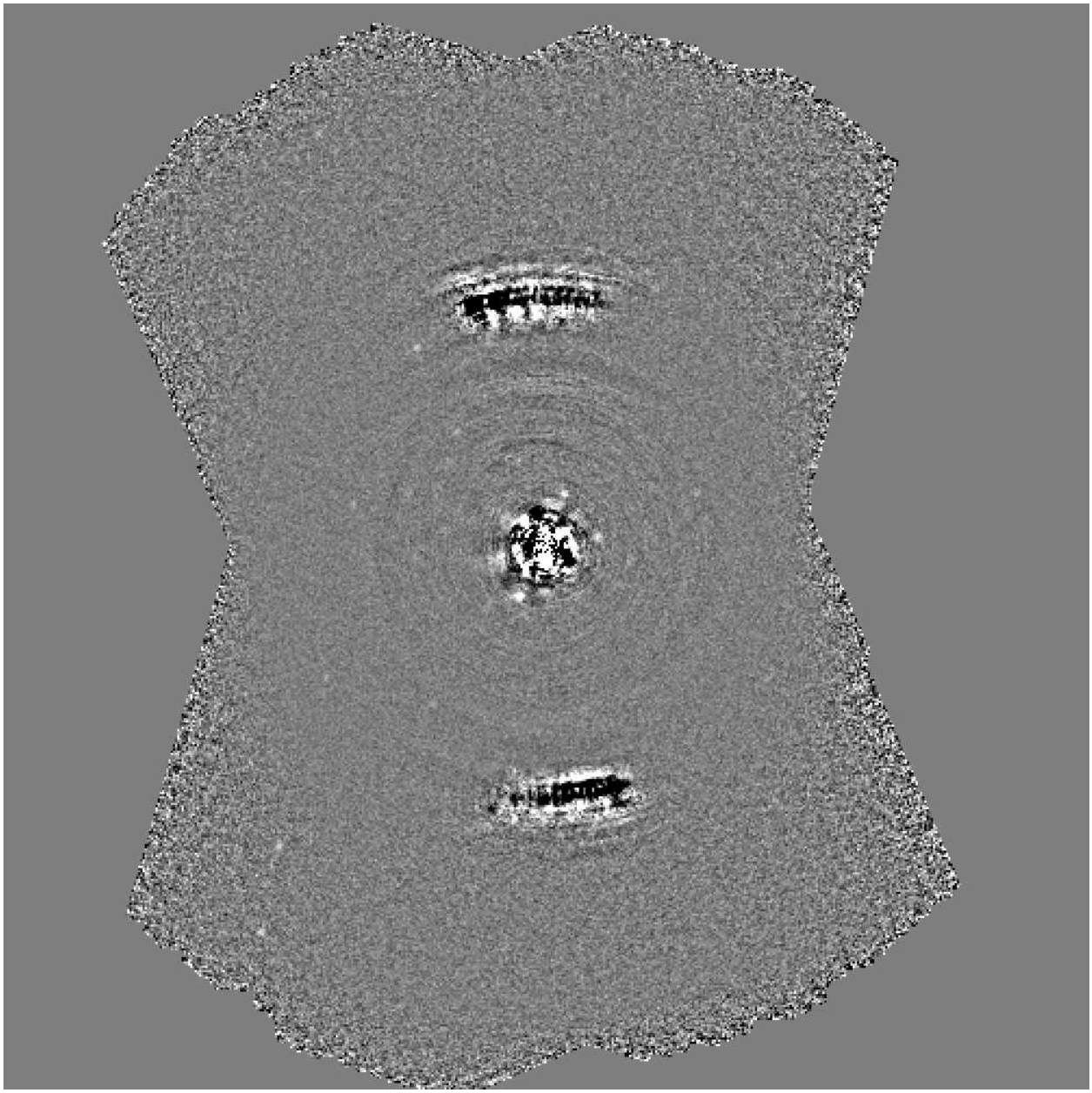

Fig. 9.— Fully processed 'e' method master image from the blind sensitivity test on HD 29391. Identifying the simulated planets is left as an exercise for the reader. The contrast stretch chosen here makes visible all the planets except the innermost and brightest ones, which are lost in speckle noise that saturates the image display range. In this data set there are 12 planets of 10σ significance, 10 at 7σ, and 5 at 5σ

Table 10. Confirmed Sources in Our Survey

Star Name	Det. Sig.	L' Mag	Sep (asec)	PA	Date Obs
GJ 354.1A	4.93σ	16.37	4.93	187.3°	06/04/12
GJ 564	175.68σ	10.80	2.60	103.0°	06/04/13
GJ 3876	246.38σ	10.88	1.85	118.6°	06/04/13
GJ 3860	19.21σ	14.53	9.68	144.4°	06/06/09
61 Cyg A	···	12.43	11.24	227.5°	06/06/09
61 Cyg A	32.82σ	13.05	7.78	83.2°	06/06/09
61 Cyg B	···	14.04	9.85	145.4°	06/06/10
BD+60 1417	11.91σ	15.70	1.93	301.4°	06/06/10
GJ 684 A	7.23σ	15.00	3.01	358.5°	06/06/11
GJ 860 A	···	15.76	7.24	0.25°	06/06/12
BD+20 1790	31.51σ	14.41	8.73	74.1°	07/01/04
BD+20 1790	···	15.16	6.42	336.4°	07/01/04
HD 96064A	43.18σ	13.72	5.57	212.8°	07/01/04

Note. — The detection significance column gives the highest significance with which the source was automatically detected on any image with any method. Blanks in this column imply sources that were detected only manually. Uncertainties on the astrometry are about 0.05 asec or less; note that the position angle values of close-in companions are thus more uncertain than those of distant ones. Photometry is accurate to roughly 0.2 magnitudes; the photometry of GJ 564 is probably too faint because the aperture correction will not have been accurate for this close binary.

to proper motion confirmation.

We note that the sources around HD 96064 A and BD+60 1417 were independently detected in the Lafrenière et al. (2007) survey, and confirmed to be background objects based on proper motions. The HD 96064 A source looks double in our data, and was confirmed to be so by Lafrenière et al. (2007).

The companion of GJ 354.1 A is confirmed to be a background star rather than a common proper motion companion based on an image by Lowrance et al. (2005). The fainter of the two companions of BD+20 1790 is similarly shown to be a background object by an archival HST image. The companions of 61 Cyg A and B are background objects based on detections on POSS plates from 1991, when, due to the 61 Cyg system's fast proper motion, the objects were much farther from the bright stars and therefore beyond the glare on the POSS images. The companion of GJ 860 is confirmed to be a background star based on previous detections on POSS plates from 1953, and optical images of our own taken with the University of Arizona 1.5m Kuiper Telescope in 2005 (the latter simply prove the object is too bright in the optical to be a planet). The POSS position match is imperfect, and our optical detection is at low significance, but taken together they confirm the object's nature. The companion of GJ 684 is shown to be a background star based on proper motion in followup images we obtained using Clio in September 2008.

Figures 10 through 15 show all of our detected companions, except the companion of HD 96064, which has already been shown in Figure 2. Each of these images is from a 'd' method reduction of long exposure science data.

5.2. The Low-Mass Star GJ 3867 B

The single discovery of our survey is the low-mass stellar companion of GJ 3876. We first detected it on L' images from April 13, 2006, and confirmed it as a common proper motion companion in L', M, and K_S images taken on April 11, 2007. Table 5.2 gives our photometric and astrometric results, complete with what the object's position should have been in April 2007 if it were a background star.

GJ 3876 B is clearly a common proper motion companion. The distance to the primary star is about 43 pc, based on the parallax from Perryman et al. (1997). This translates to a projected separation of about 80 AU, which suggests and orbital period of around 700 yr for a one solar mass primary. The constant position angle over a year seems inconsistent with a face-on orbit at this period, while the formally insignificant increase in separation may hint at motion in a more inclined orbit – however, much more data is needed.

Again using the Perryman et al. (1997) distance, the K_S absolute magnitude of GJ 3876 B is 8.33 ± 0.22. Based on the models of Baraffe et al. (1998), this translates into a mass of about $0.15 \pm 0.01 M_\odot$. This estimate could be further investigated using our L' and M band magnitudes,

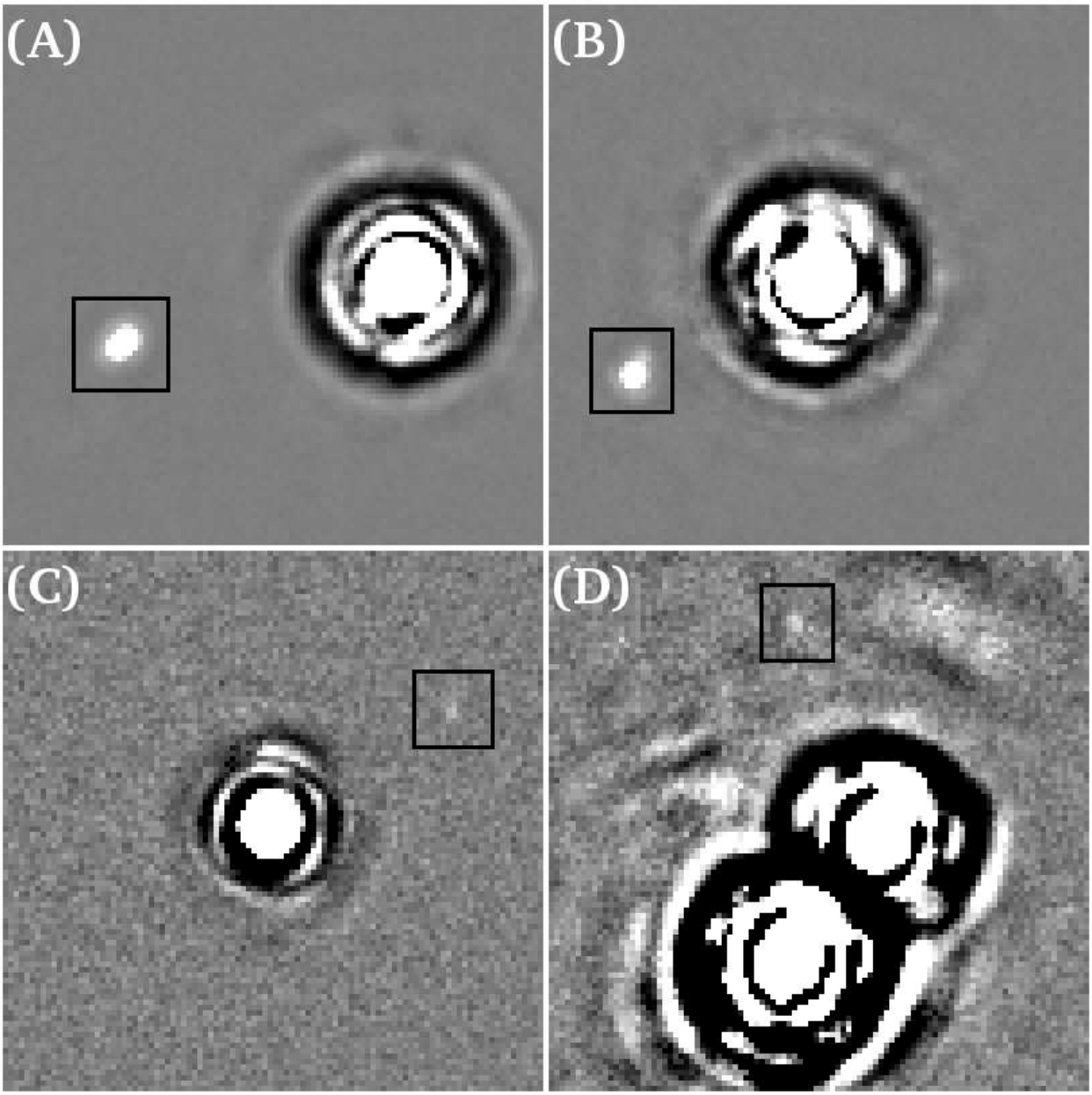

Fig. 10.— (A) L' image of GJ 564, showing the binary brown dwarf discovered by Potter et al. (2003). (B) L' image of GJ 3876, showing the low-mass stellar companion we discovered. (C) L' image of BD+60 1417, showing the faint background star we detected. (D) L' image of binary star GJ 684, showing the faint background star we detected. Each tile is 4.86 arcsec square; the bottom tiles are contrast stretched 10× more than the top ones to reveal the faint companions.

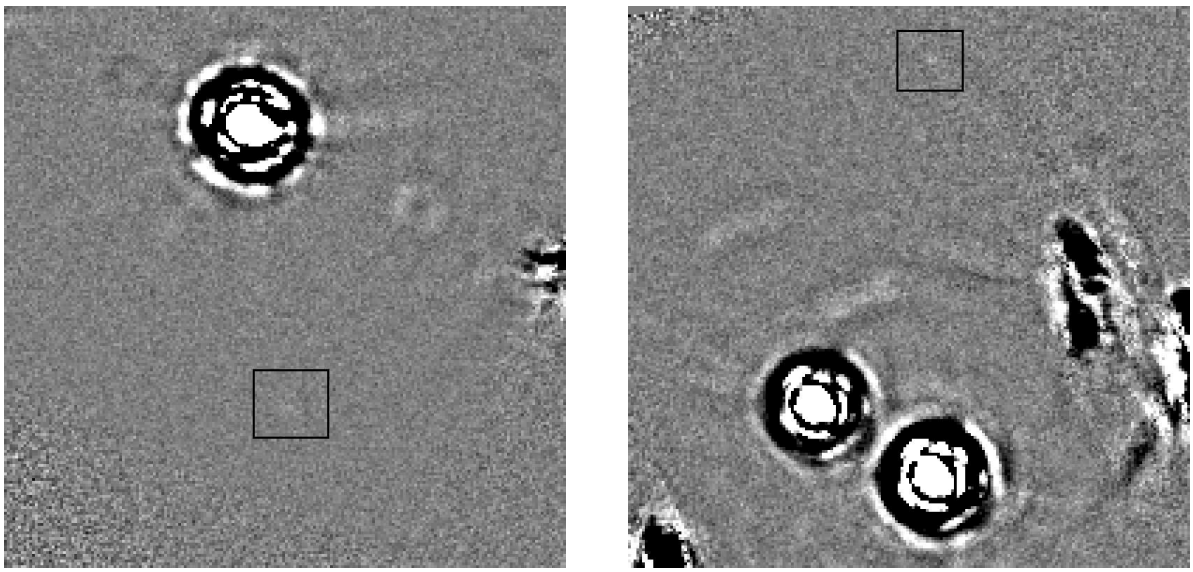

Fig. 11.— Left, L' image of GJ 354.1 A, showing the faint background star we detected. Right, L' image of binary star GJ 860, again showing a faint background star. Each image is 9.71 arcsec square, contrast stretched the same as the lower panels in Figure 10 to reveal the faint objects.

Table 11. Discovery Data for GJ 3876 B

Date (yy/mm/dd)	Sep (arcsec)	PA (degrees)	K_S	L'	M
06/04/13	1.8518 ± 0.0038	118.57 ± 0.19	···	10.88 ± 0.06	···
07/04/11	1.8603 ± 0.0082	118.64 ± 0.24	11.51 ± 0.22	10.79 ± 0.08	10.91 ± 0.28
Background	1.6487	113.73	···	···	···

Note. — Astrometry and photometry of the single discovery of our survey, GJ 3876 B. The first two rows give actual measured values; the last gives the predicted position for 07/04/11 if the object were a background star, based on the 06/04/13 position and a proper motion measurement from Perryman et al. (1997). The background star hypothesis is rejected with great confidence.

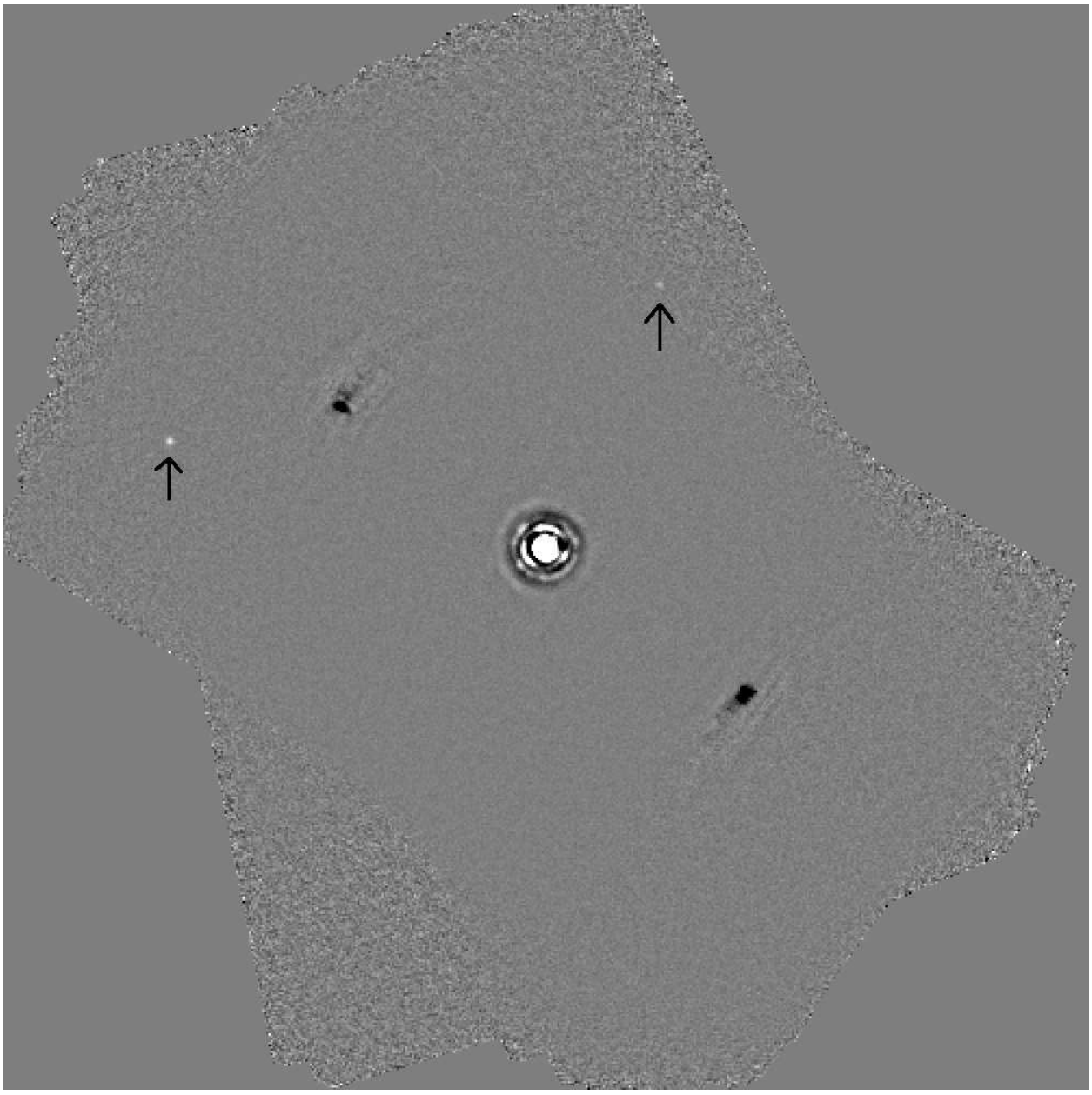

Fig. 12.— L' image of BD+20 1790, showing two faint background stars. Image is 24.29 arcsec square, contrast stretched 3× less than the images in Figure 11, to give a clear view of these somewhat brighter stars.

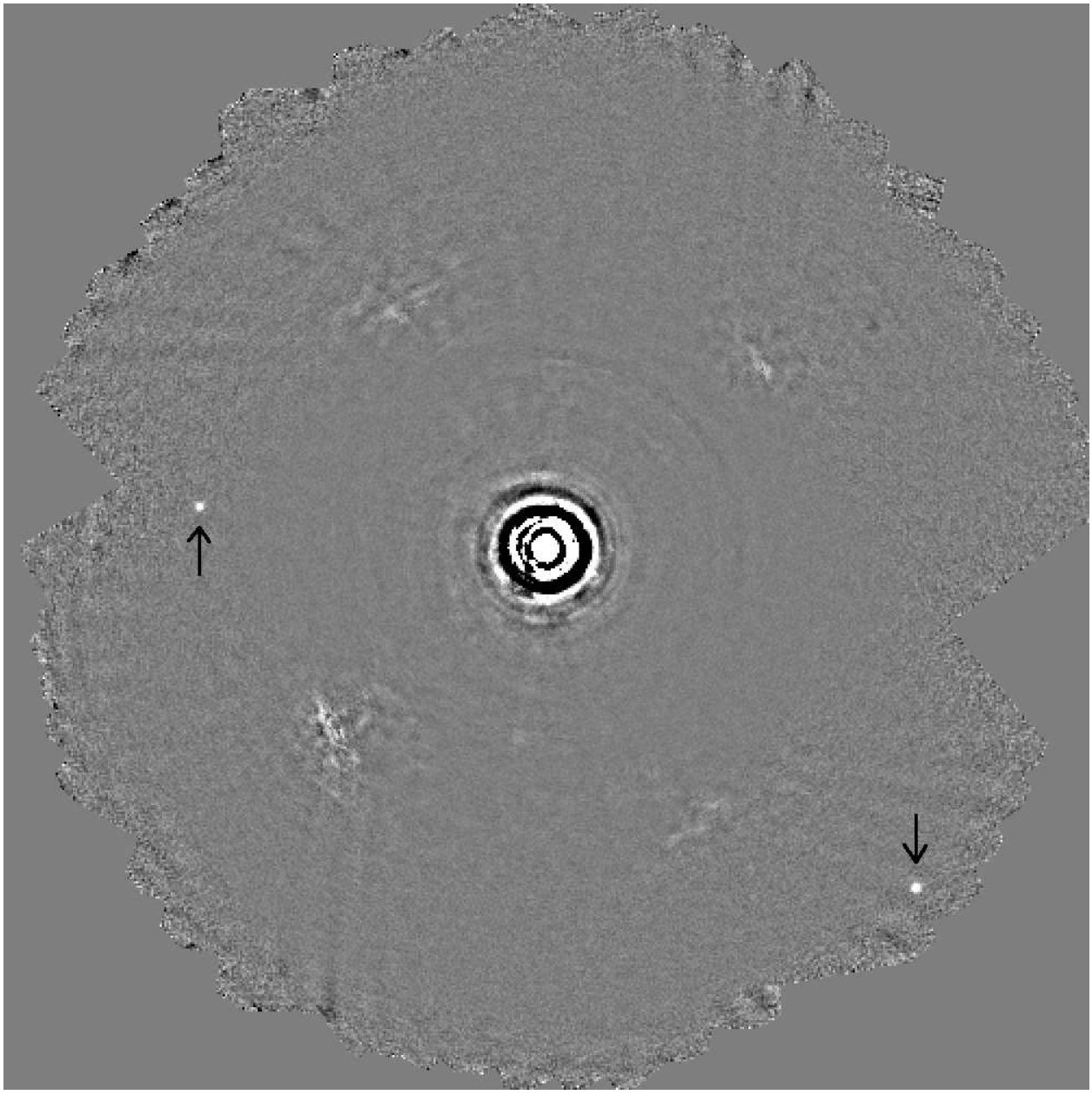

Fig. 13.— L' image of 61 Cyg A, showing two faint background stars. Image is 24.29 arcsec square, contrast stretched the same as the previous figure.

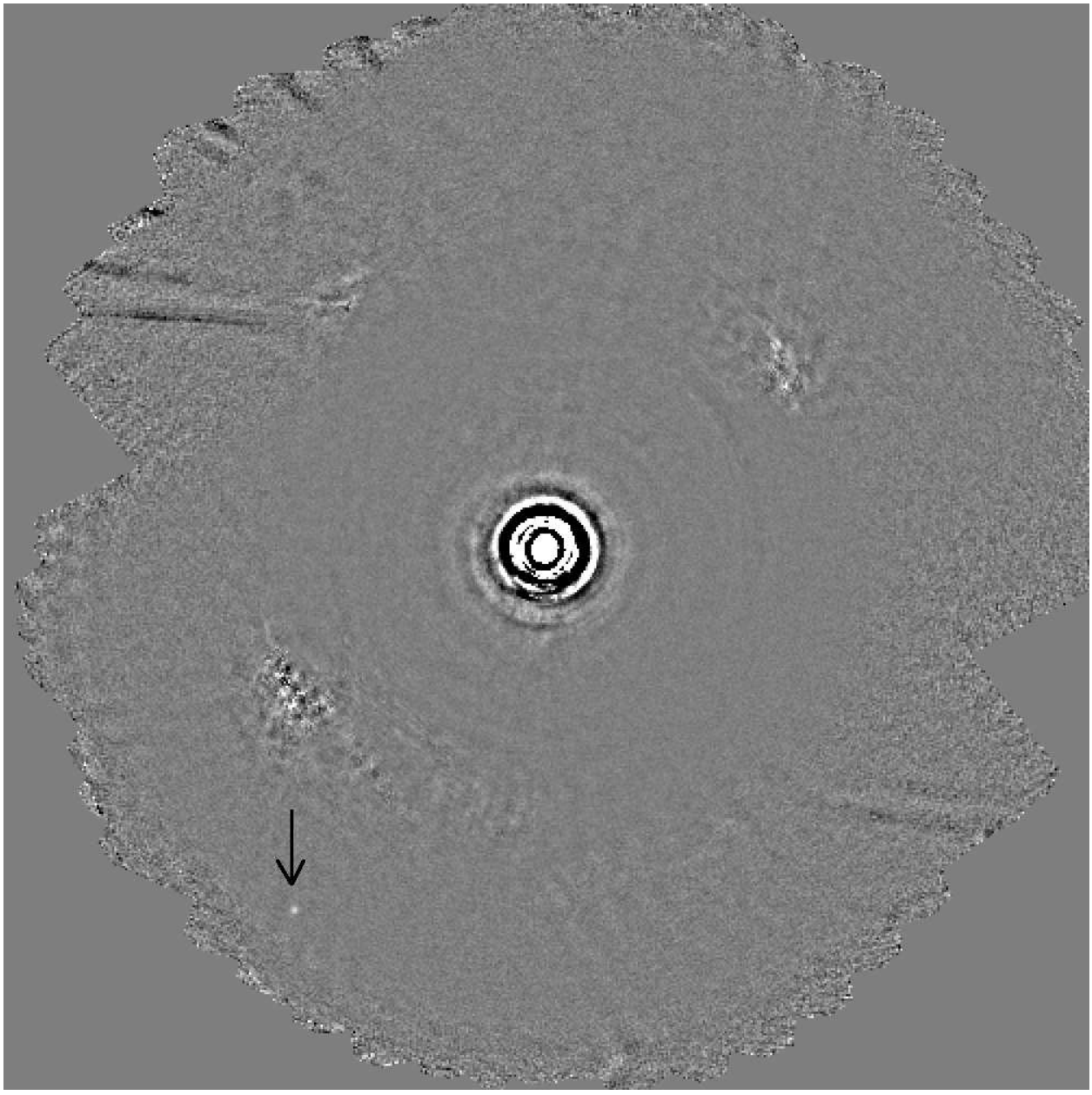

Fig. 14.— L' image of 61 Cyg B, showing a faint background star. Image is 24.29 arcsec square, contrast stretched the same as the previous figure.

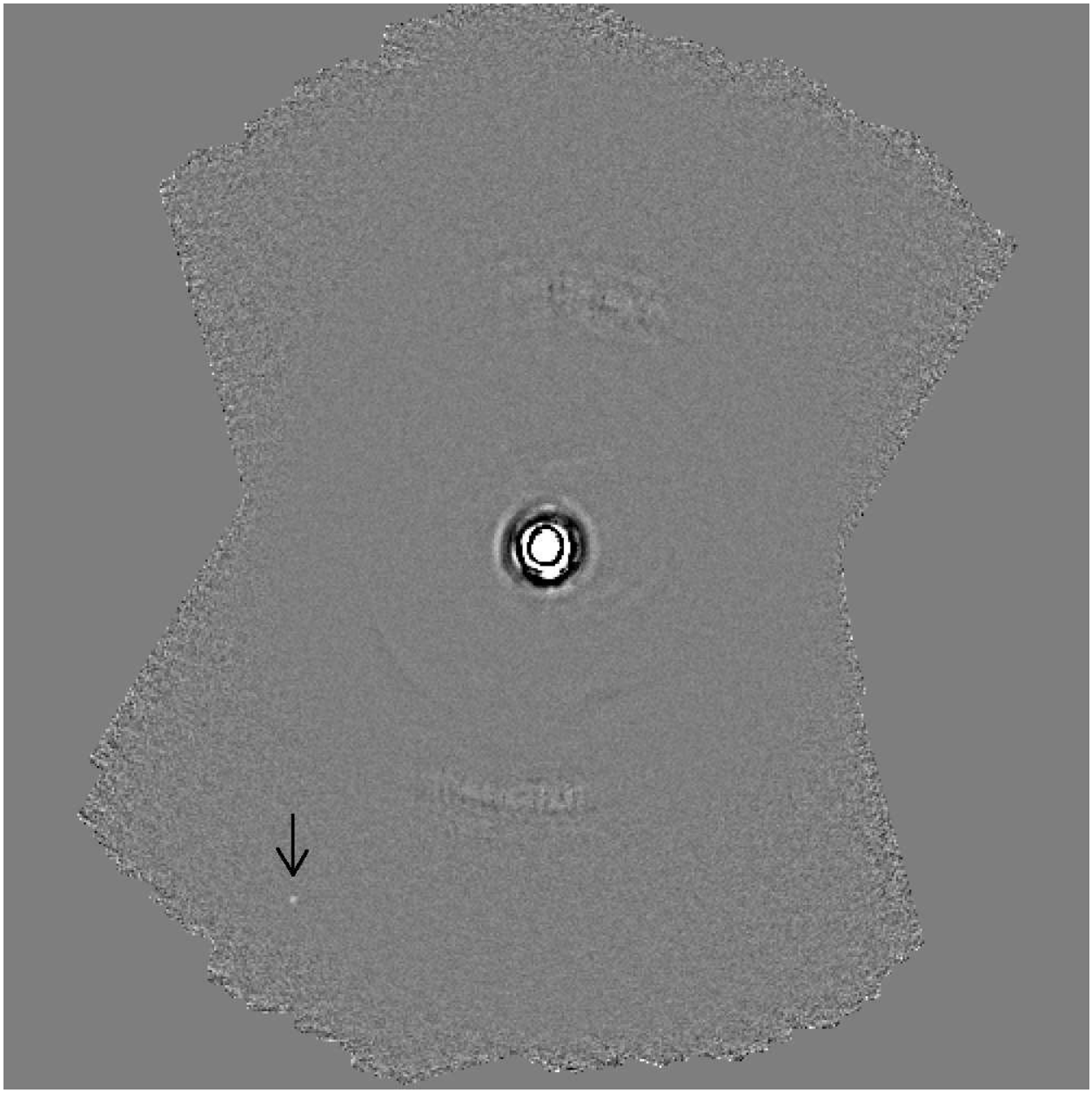

Fig. 15.— L' image of GJ 3860, showing a faint background star. Image is 24.29 arcsec square, contrast stretched the same as the previous figure.

but model magnitudes for low mass stars in these bands are not readily available in the literature, and integrating them from theoretical spectra is beyond the scope of a paper focused on planets.

6. Statistical Distributions from RV Planets

Nearly 300 RV planets are known. See Butler et al. (2006) for a useful, conservative listing of confirmed extrasolar planets as of 2006, or http://exoplanet.eu/catalog-RV.php for a frequently-updated catalog of all confirmed and many suspected extrasolar planet discoveries.

The number of RV planets is sufficient to make meaningful statistical analyses of how extrasolar planets are distributed in terms of their masses and orbital semimajor axes. The lowest mass planets and those with the longest orbital periods are generally rejected from such analyses to reduce bias from completeness effects, but there remains a considerable range (2-2000 days in period, or roughly 0.03-3.1 AU in semimajor axis for solar-type stars; and 0.5-20 MJ in mass) where RV searches have good completeness. There is evidence that the shortest period planets, or 'hot Jupiters,' represent a separate population, a 'pileup' of planets in very close-in orbits that does not follow the same statistical distribution as planets in more distant orbits (Cumming et al. 2008). The hot Jupiters are therefore often excluded from statistical fits to the overall populations of extrasolar planets, or at least from the fits to the semimajor axis distribution.

Cumming et al. (2008) characterize the distribution of RV planets detected in the Keck Planet Search with an equation of the form

$$dN = C_0 M^{\alpha_L} P^{\beta_L} d\ln(M) d\ln(P). \tag{2}$$

where M is the mass of the planet, P is the orbital period, and C_0 is a normalization constant. They state that 10.5% of solar-type stars have a planet with mass between 0.3 and 10 MJ and period between 2 and 2000 days, which information can be used to derive a value for C_0 given values for the power law exponents α_L and β_L. They find that the best-fit values for these are $\alpha_L = -0.31 \pm 0.2$ and $\beta_L = 0.26 \pm 0.1$, where the $_L$ subscript is our notation to make clear that these are the exponents for the form using logarithmic differentials.

In common with a number of other groups, we choose to represent the power law with ordinary differentials, and to give it in terms of orbital semimajor axis a rather than orbital period P:

$$dN = C_0 M^{\alpha} a^{\beta} dM da. \tag{3}$$

Where C_0, of course, will not generally have the same value for Equations 2 and 3. Manipulating the two equations and using Kepler's Third Law makes it clear that

$$\alpha = \alpha_L - 1. \tag{4}$$

and

$$\beta = \frac{3}{2}\beta_L - 1. \tag{5}$$

The Cumming et al. (2008) exponents produce $\alpha = -1.31 \pm 0.2$ and $\beta = -0.61 \pm 0.15$ when translated into our form. The mass power law is well behaved, but the integral of the semimajor axis power law does not converge as $a \to \infty$, so an outer truncation radius is an important parameter of the semimajor axis distribution.

The excellent paper presenting the 2006 Catalog of Nearby Exoplanets (Butler et al. 2006) carefully describes a heterogenous sample of extrasolar planets detected by several different RV search programs. With appropriate caution, Butler et al. (2006) refrain from quoting confident power law slopes based on the combined discoveries of many different surveys with different detection limits and completeness biases (in contrast, the Cumming et al. (2008) analysis was restricted to stars in the Keck Planet Search, which were uniformly observed up to a given minimum baseline and velocity precision). Butler et al. (2006) do tentatively adopt a power law with the form of Equation 3 for mass only, and state that α appears to be about -1.1 (or -1.16, to give the exact result of a formal fit to their list of exoplanets). However they caution that due to their heterogeneous list of planets discovered by different surveys, this power law should be taken more as a descriptor of the known planets than of the underlying distribution. They do not quote a value for the semimajor axis power law slope β.

Based mostly on Cumming et al. (2008), but considering Butler et al. (2006) as helpful additional input, we conclude that the true value of the mass power law slope α is probably between -1.1 and -1.51, with -1.31 as a good working model. The value of the semimajor axis power law slope β is probably between -0.46 and -0.76, with -0.61 as a current best guess. The outer truncation radius of the semimajor axis distribution cannot be constrained by the RV results: surveys like ours exist, in part, to constrain this interesting number.

The only other result we need from the RV searches is a normalization that will allow us to find C_0. We elect not to use the Cumming et al. (2008) value (10.5% of stars having a planet with mass between 0.3 and 10 MJ and period between 2 and 2000 days), because this range includes the hot Jupiters, a separate population.

We take our normalization instead from the Carnegie Planet Sample, as described in Fischer & Valenti (2005). Their Table 1 (online only) lists 850 stars that have been thoroughly investigated with RV. They state that all planets with mass at least 1 MJ and orbital period less than 4 years have been detected around these stars. Forty-seven of these stars are marked in Table 1 as having RV planets. Table 2 from Fischer & Valenti (2005) gives the measured properties of 124 RV planets,

including those orbiting 45 of the 47 stars listed as planet-bearing in Table 1. The stars left out are HD 18445 and and HD 225261. We cannot find any record of these stars having planets, and therefore as far as we can tell they are typos in Table 1.

Since all planets with mass above 1 MJ and period less than 4 years orbiting stars in the Fischer & Valenti (2005) list of 850 may be relied upon to have been discovered, we may pick any sub-intervals in this range of mass and period, and divide the number of planets falling into these intervals by 850 to obtain our normalization. We selected the range 1-13 MJ in mass, and 0.3-2.5 AU in semimajor axis. Twenty-eight stars, or 3.29% of the 850 in the Fischer & Valenti (2005) list, have one or more planets in this range. Our inner limit of 0.3 AU excludes the hot Jupiters, and thus the 3.29% value provides our final normalization. We note that if we adopt the Cumming et al. (2008) best-fit power laws, and use the 3.29% normalization to predict the percentage of stars having planets with masses between 0.3 and 10 MJ and orbital periods between 2 and 2000 days, we find a value of 9.3%, which is close to the Cumming et al. (2008) value of 10.5%. The slight difference is probably not significant, but might be viewed as upward bias in the Cumming et al. (2008) value due to including the hot Jupiters.

Juric & Tremaine (2007) provide a helpful mathematical description of the eccentricity distribution of known RV planets:

$$P(\epsilon) = \epsilon e^{-\epsilon^2/(2\sigma^2)}. \tag{6}$$

where $P(\epsilon)$ is the probability of a given extrasolar planet's having orbital eccentricity ϵ, e is the root of the natural logarithm, and $\sigma = 0.3$. In Figure 16 we show the Juric & Tremaine (2007) eccentricity distribution overlaid on a histogram of the eccentricities of 51 planets from Table 2 of Fischer & Valenti (2005) that have masses between 1 and 13 MJ and semimajor axis between 0.3 and 2.5 AU. The agreement is excellent, so we have used this eccentricity distribution for the Monte Carlo simulations we describe in Section 7 below.

7. Constraints on the Distribution of Planets

7.1. Theoretical Spectra

Burrows et al. (2003) present high resolution, flux-calibrated theoretical spectra of giant planets or brown dwarfs for ages ranging from 0.1-5.0 Gyr and masses from 1 to 20 MJ (these are available for download from http://zenith.as.arizona.edu/~burrows/). We have integrated these spectra to give absolute magnitudes in the L' and M filters used in Clio, and have found that the results can be reasonably interpolated to give the L' or M band magnitudes for all planets of interest for our survey. Baraffe et al. (2003) also present models of giant planets and brown dwarfs, pre-integrated into magnitudes in the popular infrared bands. These models predict slightly better sensitivity to low mass planets in the L' band and slightly poorer sensitivity in the M band, relative to the

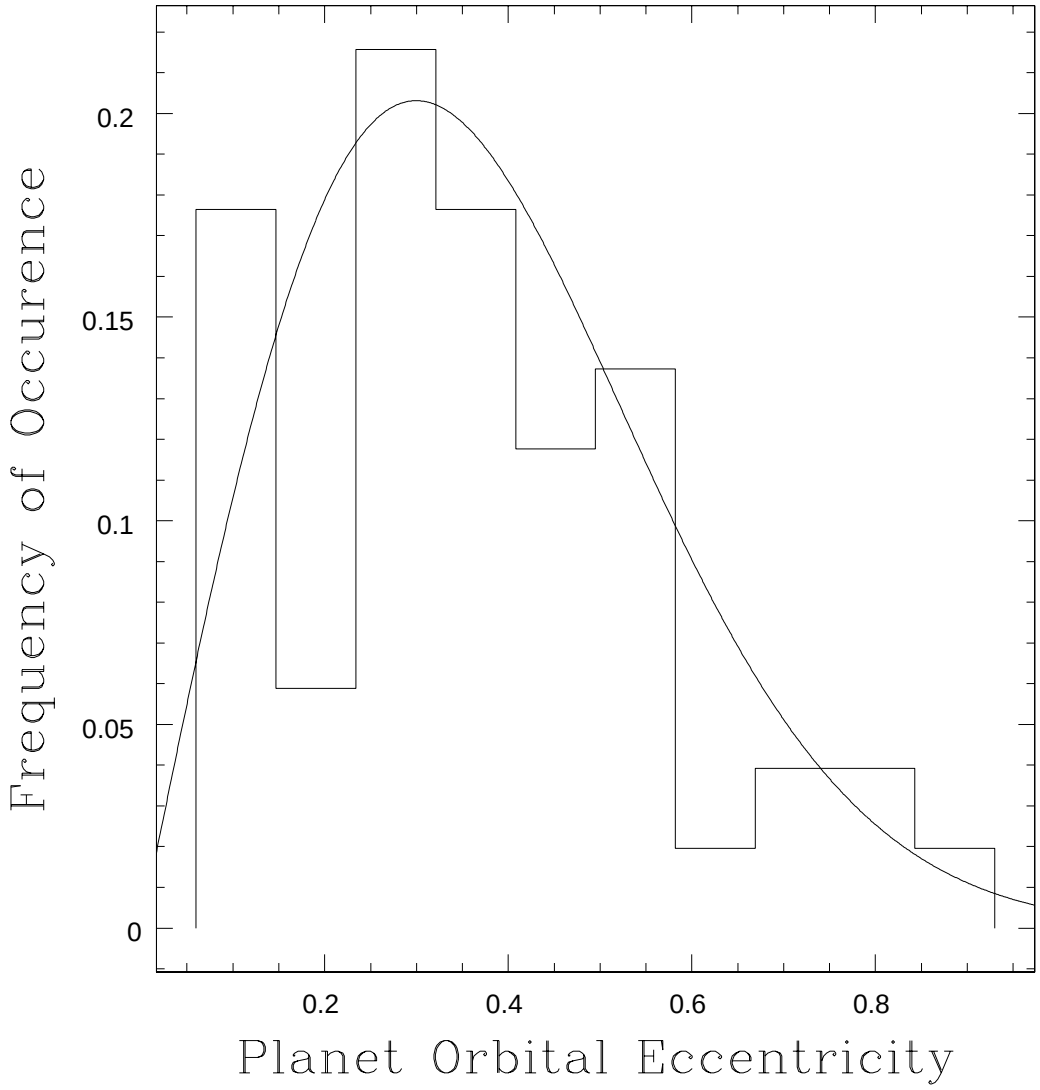

Fig. 16.— Histogram of orbital eccentricities for 51 RV planets from Fischer & Valenti (2005), with the distribution from Juric & Tremaine (2007) overplotted. The fit appears very good, hence we have used this distribution to generate eccentricities for planets in our Monte Carlo simulations.

Burrows et al. (2003) models. We cannot say if the difference is due to the slightly different filter sets used (MKO for Clio vs. Johnson-Glass and Johnson for Baraffe et al. (2003)), or if it is intrinsic to the different model spectra used in Burrows et al. (2003) and Baraffe et al. (2003). We have chosen to use the Burrows et al. (2003) models exclusively herein, to avoid any errors due to the slight filter differences. Since the Burrows et al. (2003) models predict less good sensitivity in the L' band, in which the majority of our survey was conducted, our decision to use them is conservative.

7.2. Introducing the Monte Carlo Simulations

In common with several other surveys (Kasper et al. 2007; Biller et al. 2007; Lafrenière et al. 2007) we have used our survey null result to set upper limits on planet populations via Monte Carlo simulations. In these simulations, we input our sensitivity data in the form of tabular files giving the sensitivity in apparent magnitudes as a function of separation in arcseconds for each star. Ten different sensitivity percentiles are calculated at each radius, as described in Section 4.1 above.

Each Monte Carlo simulation requires as input the planet distribution power law slopes α and β, and an outer truncation value R_{trunc} for the semimajor axis distribution. Using the normalization described in Section 6, the probability P_{plan} of any given star having a planet between 1 and 20 MJ is then calculated from the input α, β, and R_{trunc}. In each realization of our survey, each star is randomly assigned a number of planets, based on Poisson statistics with mean P_{plan}. In most cases $P_{plan} << 1$, so the most likely number of planets is zero. If the star is found to have one or more planets, the mass and semimajor axis of each are randomly selected from the input power law distributions. The eccentricity is randomly selected from the Juric & Tremaine (2007) distribution, and an inclination is randomly selected from the distribution $P(i) \propto \sin(i)$. If the star is a binary, the planet may be dropped from the simulation at this point if the orbits seems likely to be unstable. In general we consider circumstellar planets to be stable as long as their apastron distance is less than 1/3 the projected distance to the companion star, and circumbinary planets to be stable as long as their periastron distance is at least 3× greater than the projected separation of the binary. For planets orbiting low-mass secondaries, a smaller limit on the apastron distance is sometimes imposed, while often circumbinary planets required such distant orbits that they were simply not considered; the details are given in Table 14. For each planet passing the orbital stability checkpoint, a full orbit is calculated using a binary star code by M. K. The projected separation in asec is found, and the magnitude of the planet is calculated from its mass, distance, and age using the Burrows et al. (2003) models.

Finally, two random choices decide to what sensitivity value the planet's predicted magnitude will be compared. First, one of the ten percentiles given in the sensitivity files is randomly selected. Then, it is determined if the planet will be detectable at 5σ, 7σ, or 10σ. The probabilities here follow the completeness levels: 16% chance the planet will be evaluated against the 5σ sensitivity; if this option is not selected, an additional 30% chance the planet will be evaluated against 7σ; if this option is not selected either, the planet will be evaluated against 10σ. Note that although we

Table 12. L' Band Absolute Mags from Burrows et al. (2003)

Planet Mass in MJ	Mag at 0.10 Gyr	Mag at 0.32 Gyr	Mag at 1.0 Gyr	Mag at 3.2 Gyr	Mag at 5.0 Gyr
1.0	19.074	23.010	27.870	33.50[a]	35.50[a]
2.0	16.793	19.351	23.737	28.398	29.479
5.0	14.500	16.397	18.588	22.437	24.407
7.0	13.727	15.390	17.336	20.131	21.574
10.0	12.888	14.437	16.246	18.480	19.466
15.0	12.00[b]	13.61[b]	14.773	16.816	17.691
20.0	11.30[b]	12.98[b]	14.190	15.967	16.766

[a]No models for these very faint planets appear in Burrows et al. (2003). We have inserted ad hoc values to smooth the interpolations. Any effect of the interpolated magnitudes for planets we could actually detect is negligible.

[b]No models for these bright, hot planets appear in Burrows et al. (2003), which focuses on cooler objects. We have added values from Baraffe et al. (2003) and then adjusted them to slightly fainter values to insure smooth interpolations.

Table 13. M Band Absolute Mags from Burrows et al. (2003)

Planet Mass in MJ	Mag at 0.10 Gyr	Mag at 0.32 Gyr	Mag at 1.0 Gyr	Mag at 3.2 Gyr	Mag at 5.0 Gyr
1.0	14.974	16.995	19.987	25.0[a]	26.0[a]
2.0	14.023	15.313	17.807	21.295	22.163
5.0	13.014	14.017	15.153	17.167	18.537
7.0	12.618	13.561	14.558	16.126	16.909
10.0	12.189	13.096	14.093	15.315	15.951
15.0	11.55[b]	12.60[b]	13.370	14.512	14.990
20.0	11.29[b]	12.21[b]	13.069	14.122	14.580

[a]No models for these very faint planets appear in Burrows et al. (2003). We have inserted ad hoc values to smooth the interpolations. Any effect of the interpolated magnitudes for planets we could actually detect is negligible.

[b]No models for these bright, hot planets appear in Burrows et al. (2003), which focuses on cooler objects. We have added values from Baraffe et al. (2003) and then adjusted them to slightly fainter values to insure smooth interpolations.

had 97% completeness at 10σ, we have elected to let all simulated planets be evaluated at least compared to 10σ, because at only slightly above 10σ the true completeness certainly becomes 100% for all practical purposes. Note that the random step deciding at what significance level to evaluate the planet is independent of what the actual brightness of the planet might be. For example, the 10σ sensitivity at a planet's location might be $L' = 15.3$, in which case the planet would have a 16% chance of being evaluated against a sensitivity of $L' = 16.05$ (5σ), a 30% chance of being evaluated against $L' = 15.69$ (7σ), and a 54% chance of being evaluated against $L' = 15.3$. However, the simulated planet's brightness could be anything: for example, $L' = 14.2$ (sure to be detected), or $L' = 19.8$ (sure to be undetected).

7.3. A Detailed Look at a Monte Carlo Simulation

To evaluate the significance of our survey and provide some guidance for future work, we have analyzed in detail a single Monte Carlo simulation. We chose the Cumming et al. (2008) best fit values of $\alpha = -1.31$ and $\beta = -0.61$, with the semimajor axis truncation radius set to 100 AU. The simulation consisted of 50,000 realizations of our survey with these parameters.

In 38% of these simulated cases, our survey found zero planets, while 37% of the time it found one, and 25% of the time it found two or more. The planet distribution we considered in this simulation cannot be ruled out by our survey, since a null result such as we actually obtained turns out not to be very improbable.

The median mass of planets detected was 11.36 MJ, the median semimajor axis was 43.5 AU, the median angular separation was 2.86 asec, and the median significance was 21.4σ. This last number is interesting because it suggests that, for our survey, any real planet detected was likely to appear at high significance, obvious even on a preliminary, 'quick-look' reduction of the data. Therefore, such reductions should always be performed at the telescope, to allow immediate followup if a candidate is seen.

We suspected that there would be a detection bias toward very eccentric planets, because these would spend most of their orbits near apastron, where they would be easier to detect. This bias did not appear at any measurable level in our simulation. However, there was a weak but clear bias toward planets in low-inclination orbits, which, of course, spend more of their time at large separations from their stars than do planets with nearly edge-on orbits.

A concern with any planet imaging survey is how strongly the results hinge on the best few stars. A survey of 54 stars may have far less statistical power than the number would imply if the best two or three stars had most of the probabilty of hosting detectable planets. Table 15 gives the percentage of planets detected around each star in our sample based on our detailed Monte Carlo simulation. Due to poor data quality, binary orbit constraints, or other issues, a few stars had zero probability of detected planets given the distribution used here. In general, however, the likelihood of hosting detectable planets is fairly well distributed.

In Table 14, we give precise Clio astrometry of each binary star we observed, and include the details of planetary orbital constraints used in the Monte Carlo simulations. Two binaries, ξ Boo and GJ 702, were observed twice, once in L' and once at M band. The 2σ difference in measured separation between the two ξ Boo observations is pure measurement error, since they are only one day apart. However, clear orbital motion is detected over the ten months spanned by our two measurements of GJ 702. Note that HD 96064 B is a close binary star in its own right, so planets orbiting it were limited in two ways: the apastron could not be too far out, or the orbit would be rendered unstable by proximity to HD 96064 A – but the periastron also could not be too far in, or the binary orbit of HD 96064 Ba and HD 96064 Bb would render it unstable. Planets individually orbiting HD 96064 Ba or HD 96064 Bb were not considered in our survey, since to be stable the planets would have to be far too close-in for us to detect them. The constraints described in Table 14 account for most of the stars in Table 15 with few or no detections reported.

A final question our detailed simulation can address is how important the M band observations were to the survey results. In Table 16, we show that when M band observations were made, they did substantially increase the number of simulated planets detected.

Table 14. Binary Star Data and Constraints on Simulated Planet Orbits

Star Name	Date Obs. (dd/mm/yy)	Sep.(asec)	PA(deg)	apast. cons. asec/AU	periast. cons. asec/AU
HD 220140 A	03/12/06	10.828 ± 0.007	214.49±0.20	<3.61/71.3	No Orbits
HD 220140 B				<2.17/42.8	NA
HD 96064 A	04/01/07	11.628 ± 0.007	221.61±0.20	<3.88/95.6	No Orbits
HD 96064 B				<2.33/57.3	NA
HD 96064 Ba	04/01/07	0.217 ± 0.010	26.6±4.3	No Orbits	>0.65/16.1
HD 96064 Bb				No Orbits	NA
GJ 896 A	13/07/06	5.366 ± 0.006	86.16± 0.20	<1.79/11.8	No Orbits
GJ 896 B				<1.79/11.8	NA
GJ 860 A	12/06/06	2.386 ± 0.004	58.55±0.20	<0.79/3.17	>7.15/28.7
GJ 860 B				<0.60/2.41	NA
ξ Boo A	10/06/06	6.345 ± 0.006	312.15±0.20	<2.12/14.2	No Orbits
ξ Boo B				<2.12/14.2	NA
ξ Boo A (M)	11/06/06	6.327 ± 0.005	312.14±0.20	<2.12/14.2	No Orbits
ξ Boo B (M)				<2.12/14.2	NA
GJ 166 B	03/12/06	8.781 ± 0.010	153.72±0.20	<2.20/10.6	No Orbits
GJ 166 C				<2.20/10.6	NA
GJ 684 A	11/06/06	1.344 ± 0.002	323.84±0.20	<0.45/6.34	>4.03/56.8
GJ 684 B				<0.27/3.80	NA
GJ 505 A	12/06/06	7.512 ± 0.006	104.92±0.20	<2.50/29.8	No Orbits
GJ 505 B				<2.50/29.8	NA
GJ 702 A	09/06/06	5.160 ± 0.005	135.79±0.20	<1.76/8.85	>15.9/79.7
GJ 702 B				<1.32/6.64	NA
GJ 702 A (M)	11/04/07	5.290 ± 0.004	134.69±0.20	<1.76/8.85	>15.9/79.7
GJ 702 B (M)				<1.32/6.64	NA
HD 77407 A	05/01/07	1.698 ± 0.002	356.37±0.20	<0.57/17.2	>5.11/153.7
HD 77407 B				<0.34/10.23	NA

Note. — The apastron constraints column shows the maximum apastron allowed for simulated circumstellar planets before they were rejected as unstable. The periastron constraints column shows the *minimum* periastron allowed for simulated *circumbinary* planets. In the simulation, circumbinary planets are assigned to the primary, hence this column has no meaning for the secondaries. No Orbits simply means the simulation ruled out any stable orbits of the

assigned type. Note the star HD 96064 B is itself a close binary; only circumbinary planets were considered for it.

Table 15. Percentage of Detected Planets Found Around Each Star

Star Name	% of Total Detected Planets	Median Mass	Median Semimajor Axis	Median Separation
GJ 117	6.07	7.66 MJ	39.36 AU	3.64 asec
ϵ Eri	5.83	6.98 MJ	18.26 AU	4.35 asec
HD 29391	5.80	8.14 MJ	49.13 AU	2.71 asec
GJ 519	4.74	10.44 MJ	40.51 AU	3.28 asec
GJ 625	4.67	9.72 MJ	29.18 AU	3.48 asec
GJ 5	4.45	9.60 MJ	53.42 AU	3.08 asec
BD+60 1417	3.95	11.58 MJ	44.48 AU	2.05 asec
GJ 355	3.81	9.71 MJ	53.91 AU	2.34 asec
GJ 354.1 A	3.67	9.58 MJ	60.12 AU	2.64 asec
GJ 159	3.57	9.73 MJ	57.95 AU	2.71 asec
GJ 349	3.35	11.38 MJ	44.40 AU	3.17 asec
61 Cyg B	3.29	11.32 MJ	19.53 AU	4.08 asec
GJ 879	3.03	11.18 MJ	36.84 AU	3.69 asec
GJ 564	2.94	10.67 MJ	56.80 AU	2.70 asec
GJ 410	2.93	12.78 MJ	41.83 AU	3.03 asec
GJ 450	2.89	12.90 MJ	38.72 AU	3.66 asec
GJ 3860	2.68	12.70 MJ	49.72 AU	2.69 asec
HD 78141	2.58	12.47 MJ	57.00 AU	2.24 asec
BD+20 1790	2.51	12.14 MJ	58.33 AU	2.02 asec
GJ 278 C	2.20	12.68 MJ	54.56 AU	3.04 asec
GJ 311	2.19	12.55 MJ	52.07 AU	3.20 asec
HD 113449	2.17	12.52 MJ	59.31 AU	2.29 asec
GJ 211	2.10	13.59 MJ	50.51 AU	3.30 asec
BD+48 3686	2.08	12.56 MJ	55.05 AU	2.01 asec
GJ 282 A	2.05	13.39 MJ	49.85 AU	2.99 asec
GJ 216 A	2.03	12.71 MJ	42.98 AU	4.21 asec
61 Cyg A	1.97	13.70 MJ	20.94 AU	4.54 asec
HD 1405	1.54	13.13 MJ	66.34 AU	2.04 asec
HD 220140 A	1.54	11.73 MJ	36.85 AU	1.73 asec
HD 96064 A	1.49	12.63 MJ	46.64 AU	1.75 asec
HD 139813	1.43	14.33 MJ	59.71 AU	2.37 asec
GJ 380	0.92	15.76 MJ	25.31 AU	4.21 asec

7.4. Monte Carlo Simulations: Constraining the Power Laws

The planet distribution we used in the single Monte Carlo simulation described above could not be ruled out by our survey. To find out what distributions could be ruled out, we performed Monte Carlo simulations assuming a large number of different possible distributions, parametrized by the two power law slopes α and β, and by the outer semimajor axis truncation radius R_{trunc}.

We tested three different values of α: -1.1, -1.31, and -1.51, roughly corresponding to the most optimistic permitted, the best fit, and the most pessimistic permitted values from Cumming et al. (2008). For each value of α, we ran simulations spanning a wide grid in terms of β and R_{trunc}. In constrast to the extensive results described in Section 7.3, the only data saved for these simulations was the probability of finding zero planets. Since we did in fact obtain a null result, distributions for which the probability of this was sufficiently low can be ruled out.

Figures 17 through 19 show the probability of a null result as a function of β and R_{trunc} for our three different values of α. Each pixel in these figures represents a Monte Carlo simulation involving 15,000 realizations of our survey; generating the figures took several tens of hours on a fast PC. Contours are overlaid at selected probability levels. Regions within the 1%, 5%, and 10% contours can, of course, be ruled out at the 99%, 95%, and 90% confidence levels respectively. For example, we find that $\alpha = -1.1$ and $\beta = -0.44$, truncated at 100 AU, is ruled out with 90% confidence; while $\alpha = -1.51$ and $\beta = -0.3$, truncated at 100 AU, is similarly ruled out.

7.5. Model-Independent Constraints

It is also possible to place constraints on the distribution of planets without assuming a power law or any other particular model. To place such constraints, we performed a new series of Monte Carlo simulations on a grid of planet mass and orbital semimajor axis. For each grid point we seek to determine a number $P(M, a)$ such that, with some specified level of confidence (e.g., 90%), the probability of a star like those in our sample having a planet with the specified mass M and semimajor axis a is no more than $P(M, a)$. We determine $P(M, a)$ by a search: first a guess is made, and a Monte Carlo simulation assuming this probability is performed. If more than 10% of the realizations of our survey turn up a null result, the guessed probability is too low; if less than 10% turn up a null result, the probability is too high. It is adjusted in steps of ever-decreasing size until the correct value is reached.

Figure 20 shows the 90% confidence upper limit on $P(M, a)$ as a function of mass M and semimajor axis a. Each pixel represents thousands of realizations of our survey, with $P(M, a)$ finely adjusted to reach the correct value. Contours are overplotted showing where $P(M, a)$ is less than 8%, 10%, 25%, 50%, and 75%, with 90% confidence. Note that $P(M, a)$ is a probability, rather than a fixed fraction: Even if a planet with a specified mass and semimajor axis is guaranteed to be detected if present around any star in our sample, and planets of this type exist around 6% of

Table 15—Continued

Star Name	% of Total Detected Planets	Median Mass	Median Semimajor Axis	Median Separation
GJ 896 A	0.61	12.43 MJ	6.47 AU	0.98 asec
GJ 860 A	0.38	11.58 MJ	53.26 AU	6.62 asec
τ Ceti	0.38	17.19 MJ	25.49 AU	5.52 asec
GJ 896 B	0.34	11.40 MJ	6.78 AU	1.14 asec
ξ Boo B	0.32	12.07 MJ	8.25 AU	1.36 asec
HD 220140 B	0.28	12.04 MJ	25.92 AU	1.37 asec
ξ Boo A	0.24	12.89 MJ	8.72 AU	1.50 asec
GJ 659 B	0.21	17.71 MJ	62.54 AU	2.81 asec
GJ 166 B	0.17	16.12 MJ	6.19 AU	1.34 asec
GJ 684 A	0.17	14.93 MJ	85.98 AU	4.87 asec
HD 96064 B	0.13	14.43 MJ	38.55 AU	1.60 asec
GJ 505 B	0.12	15.94 MJ	17.11 AU	1.61 asec
GJ 166 C	0.10	15.56 MJ	6.43 AU	1.52 asec
GJ 505 A	0.07	16.32 MJ	18.08 AU	1.75 asec
GJ 702 A	0.02	15.90 MJ	6.21 AU	1.50 asec
GJ 684 B	None	NA	NA	NA
GJ 860 B	None	NA	NA	NA
GJ 702 B	None	NA	NA	NA
HD 77407 A	None	NA	NA	NA
GJ 659 A	None	NA	NA	NA
GJ 3876	None	NA	NA	NA
HD 77407 B	None	NA	NA	NA

Table 16. Importance of the M Band Data

Star Name	Total simulated detections	2-band detections	L'-only detections	M-only detections
ϵ Eri	2850	46.98%	8.28%	44.74%
61 Cyg B	1610	52.73%	1.55%	45.71%
61 Cyg A	965	63.01%	22.80%	14.20%
ξ Boo B	157	61.15%	18.47%	20.38%
ξ Boo A	115	60.00%	18.26%	21.74%
GJ 702 A	9	22.22%	0.00%	77.78%

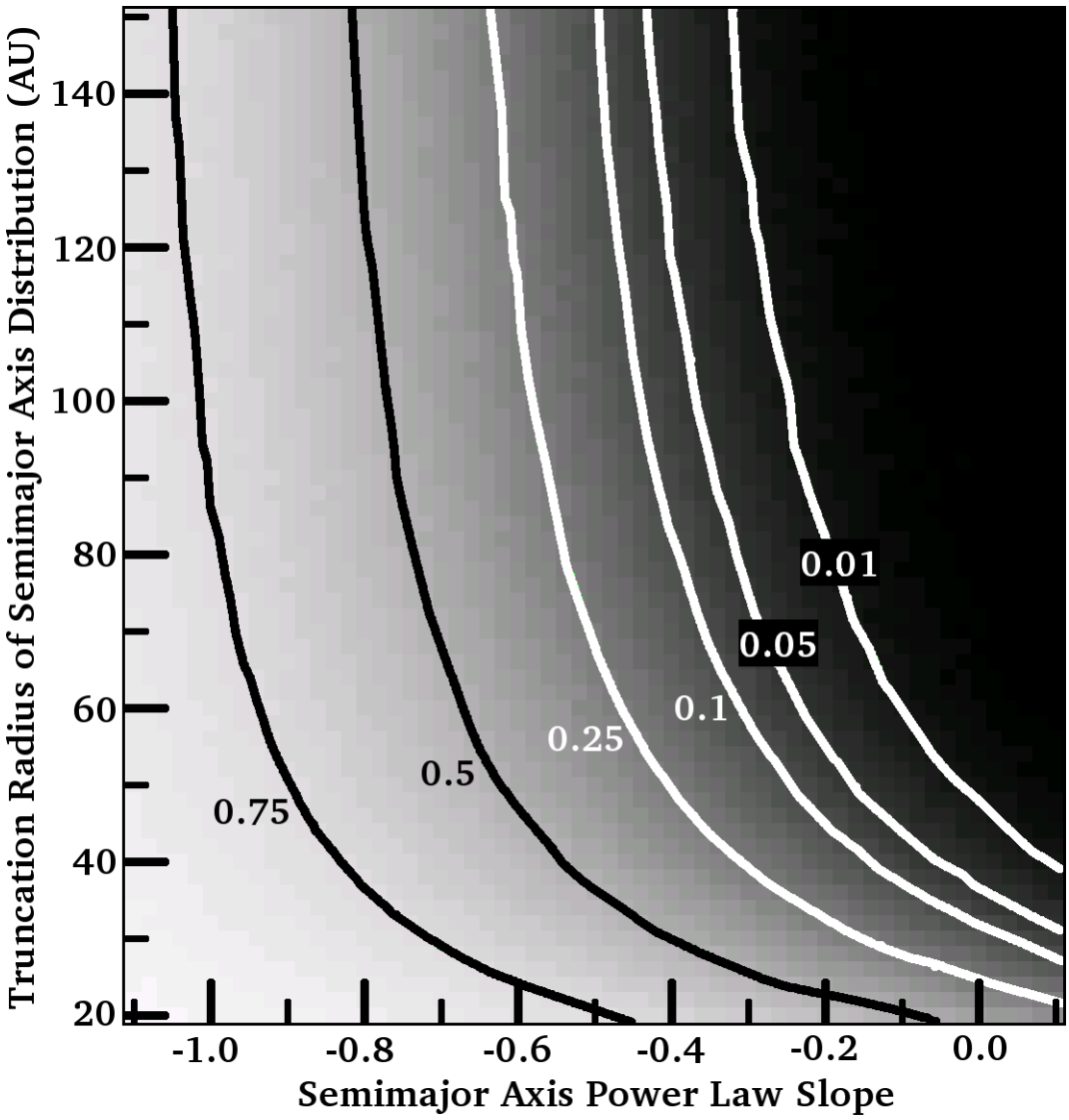

Fig. 17.— Probability of our survey detecting zero planets, as a function of the power law slope of the semimajor axis distribution β, where $\frac{dn}{da} \propto a^{\beta}$, and the outer truncation radius of the semimajor axis distribution. Here, the slope of the mass distribution α has been taken as -1.1, where $\frac{dn}{dM} \propto M^{\alpha}$. Since we found no planets, distributions that lead to a probability P of finding no planets are ruled out at the $1 - P$ confidence level: for example, the region above and to right of the 0.1 contour is ruled out at the 90% confidence level

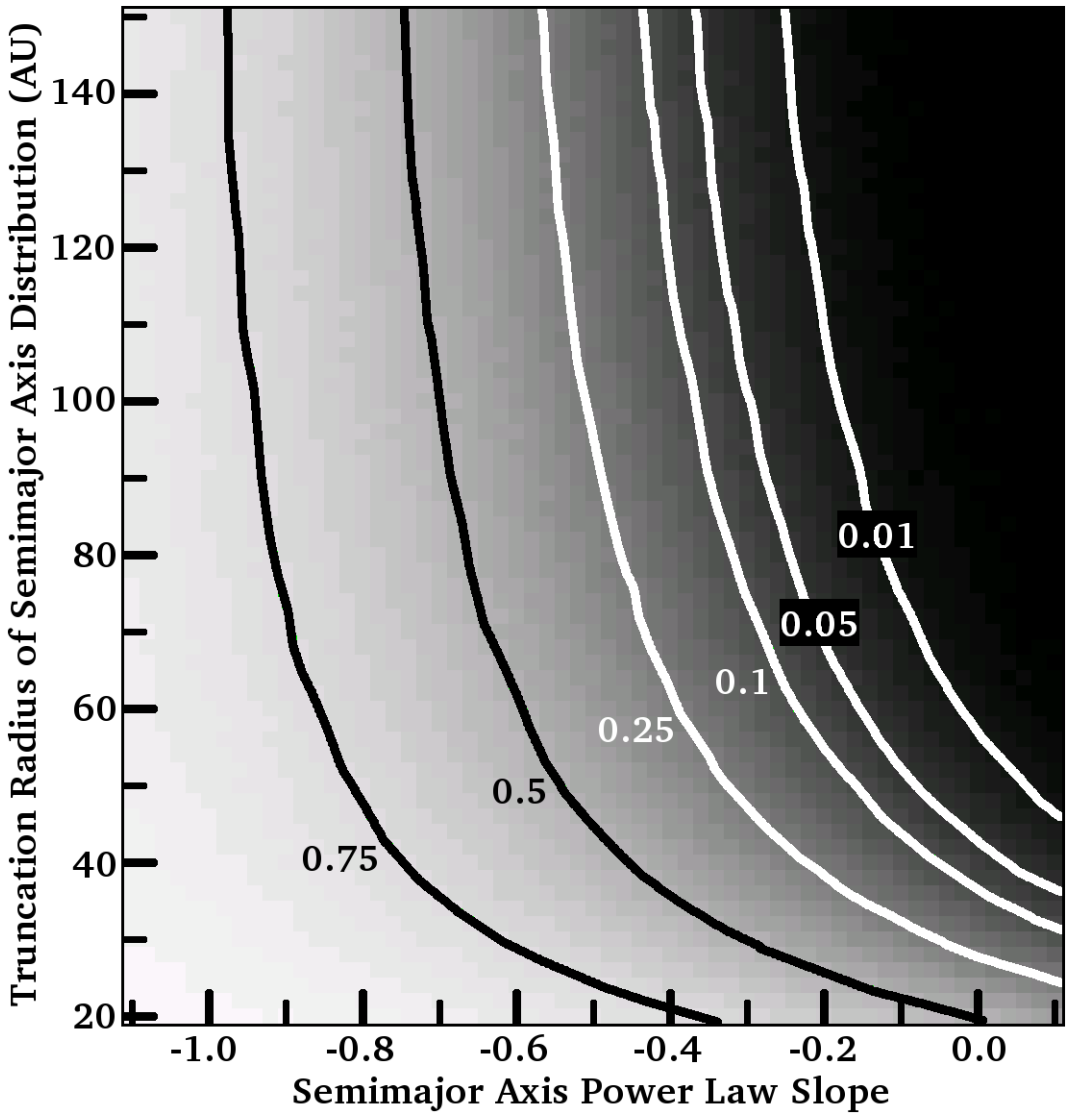

Fig. 18.— Probability of our survey detecting zero planets, as a function of the power law slope of the semimajor axis distribution β, where $\frac{dn}{da} \propto a^{\beta}$, and the outer truncation radius of the semimajor axis distribution. Here, the slope of the mass distribution α has been taken as -1.31, where $\frac{dn}{dM} \propto M^{\alpha}$. Since we found no planets, distributions that lead to a probability P of finding no planets are ruled out at the $1 - P$ confidence level: for example, the region above and to right of the 0.1 contour is ruled out at the 90% confidence level

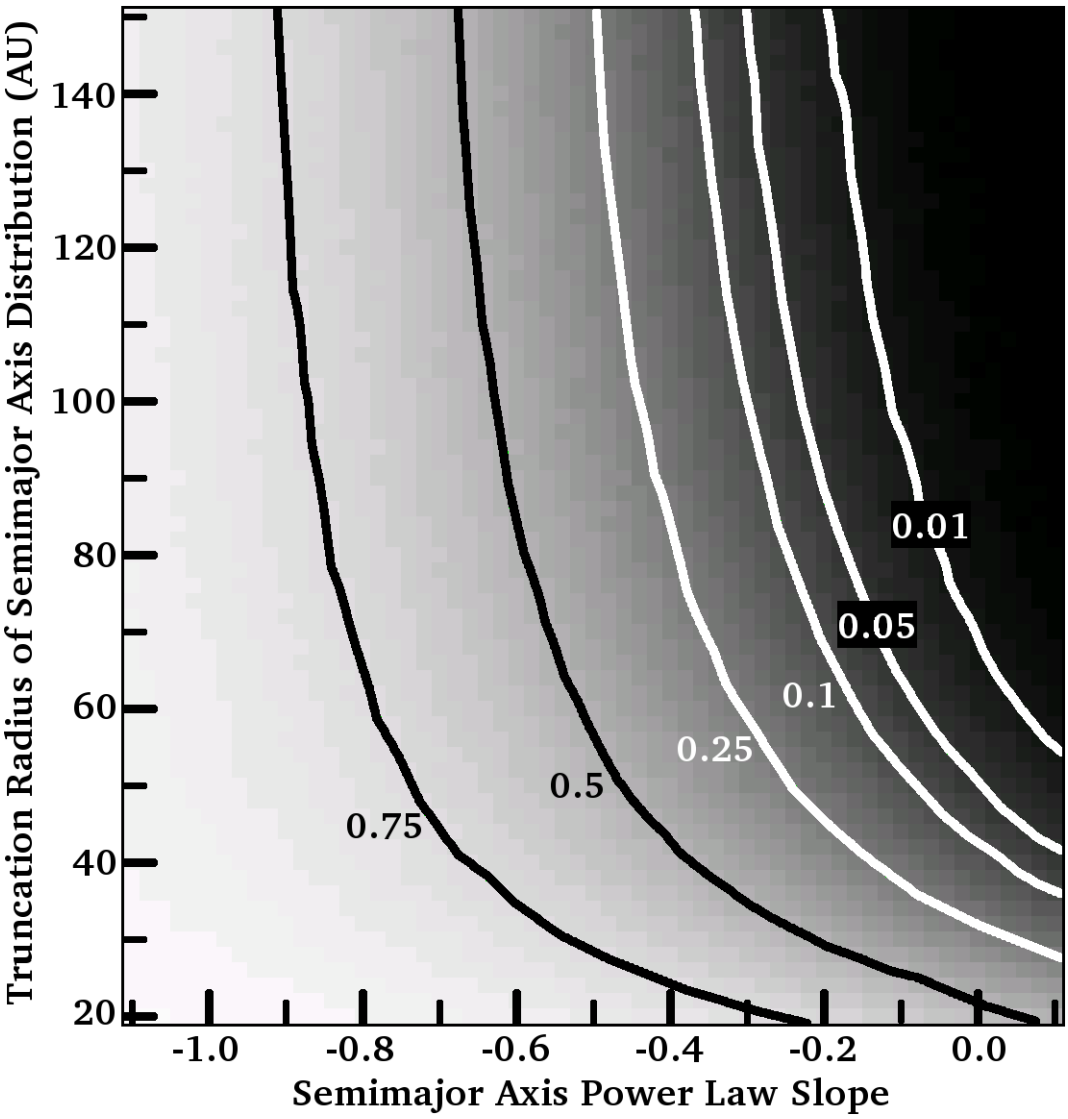

Fig. 19.— Probability of our survey detecting zero planets, as a function of the power law slope of the semimajor axis distribution β, where $\frac{dn}{da} \propto a^{\beta}$, and the outer truncation radius of the semimajor axis distribution. Here, the slope of the mass distribution α has been taken as -1.51, where $\frac{dn}{dM} \propto M^{\alpha}$. Since we found no planets, distributions that lead to a probability P of finding no planets are ruled out at the $1 - P$ confidence level: for example, the region above and to right of the 0.1 contour is ruled out at the 90% confidence level

stars, making the expected number in a 54 star survey more than 3, there is still a possibility that none of the stars in our survey will have such a planet.

Since without exception more massive planets are easier to detect, and in general planets in more distant orbits are easier to detect (until the orbits get so large that we start to lose some planets beyond our field of view), the results presented in Figure 20 can be interpreted as model-independent constraints on planet populations. For example, with 90% confidence we find that no more than 50% of stars with properties like those in our survey have a 5 MJ or more massive planet in an orbit with a semimajor axis between 30 and 94 AU. No more than 25% of stars like those in our survey have a 7 MJ or more massive planet between 25 and 100 AU, no more than 15% have a 10 MJ or more massive planet between 22 and 100 AU, and no more than 12% have a 15 MJ or more massive planet/brown dwarf between 15 and 100 AU.

We can apply a similar Monte Carlo method to that described above to set an upper limit on the occurence rate for systems of massive planets like that of HR 8799 (Marois et al. 2008). Taking the orbital radii of the planets to be 24, 38, and 68 AU, and their masses to be 10, 10, and 7 MJ, respectively, we set a 90% confidence upper limit of 8.1% on the probability of a lower-mass star like those in our survey having such a system. What the occurence rate of such systems is for more massive stars such as HR 8799 itself is not yet clear, but future surveys of both sun-like and more massive stars may confirm our current expectation that massive planets will be more abundant around massive stars.

7.6. Our Survey in the Big Picture

The surveys of Kasper et al. (2007) and Biller et al. (2007), have set constraints on the distributions of extrasolar planets similar to those we present herein, while the work of Nielsen et al. (2008) and especially Lafrenière et al. (2007) has set stronger constraints. The main importance of our work is that we targeted a different set of stars, at different wavelengths, and confirmed the conclusions of the other surveys.

The only unambiguous detections of self-luminous extrasolar planets so far are those of Marois et al. (2008), who found three massive planets in distant orbits around HR 8799. Multi-band photometry of these planets is only now being successfully obtained, and in any case they are considerably hotter than most of the planets our survey might have been expected to find. Theoretical spectra of self-luminous extrasolar planets are therefore very poorly constrained observationally.

Such models predict brightnesses in the H band, and particularly in narrow spectral windows within the H band, that are enormously in excess of black body fluxes. The constraints set by the surveys of Masciadri et al. (2005); Biller et al. (2007); Nielsen et al. (2008); and Lafrenière et al. (2007) depend on the accuracy of these models. The L' and M bands that we have used are nearer the blackbody peaks of low-temperature self-luminous planets, and might be expected to be more reliable.

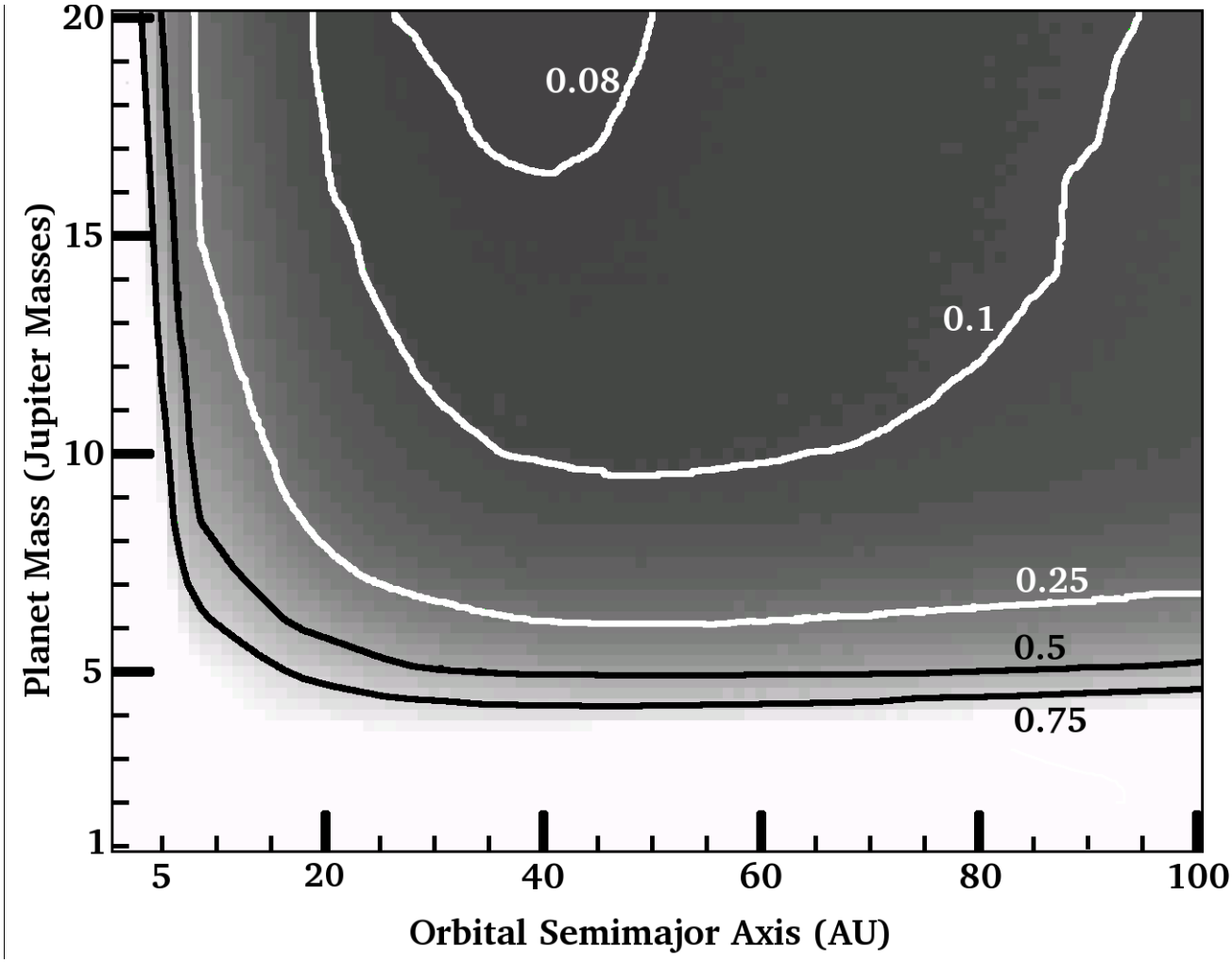

Fig. 20.— 90% confidence level upper limits on the probability of stars like those in our sample having planets with a given mass and semimajor axis.

However, Leggett et al. (2007) and Reid & Cruz (2002) suggest that the M band brightness at least of hotter extrasolar planets will be less than predicted by Burrows et al. (2003) due to above-equilibrium concentrations of CO from convective mixing. Hubeny & Burrows (2007) present new models indicating the effect diminishes for cooler planets, but it would still have some effect on our M band sensitivity. It might actually enhance the L' brightness through line-blanketing. Our conclusion is not, however, that theoretical spectra such as those of Burrows et al. (2003) are more reliable in the L' and M bands than at shorter wavelengths. Rather, so long as the models remain poorly constrained by observations at every wavelength, conclusions based on observations at multiple wavelengths will be more secure. Our survey, with that of Kasper et al. (2007), has diversified planet imaging surveys across a broader range of wavelengths.

In another sense our survey differs even from that of Kasper et al. (2007): we have investigated older stars. This is significant because planetary systems up to ages of several hundred Myr may still be undergoing substantial dynamical evolution due to planet-planet interactions (Juric & Tremaine 2007; Gomes et al. 2005). Our survey did not necessarily probe the same planet population as, for example, those of Masciadri et al. (2005) and Kasper et al. (2007). Finally, theoretical models of older planets are likely more reliable than for younger ones, as these planets are further from their unknown starting conditions and moving toward a well-understood, stable configuration such as Jupiter's. It has been suggested by Marley et al. (2007), in fact, that theoretical planet models such as those of Burrows et al. (2003) and Baraffe et al. (2003) may overpredict the brightness of young (< 100 Myr) planets by orders of magnitude, while for older planets the models are more accurate.

We have focused on nearby, mature star systems, and have conservatively handled the ages of stars. This makes our survey uniquely able to confirm that the rarity of giant planets at large separations around solar-type stars, first noticed in surveys strongly weighted toward young stars, persists at older system ages. It is not an artifact of model inaccuracy at young ages due to unknown initial conditions.

8. The Future of the L' and M Bands

In the L' and M bands, the sky brightness is much worse than at shorter wavelengths (e.g., the H band regime used by Biller et al. (2007) and Lafrenière et al. (2007)), but predicted planet/star flux ratios are better. Thus it makes sense to use these bands on bright stars, where the planet/star flux ratio is a more limiting factor than the sky brightness. In Heinze et al. (2008), we have shown that M band observations tend to do better than those at shorter wavelengths at small separations from bright stars.

The L' and M bands are also most sensitive relative to shorter wavelengths for detecting the lowest temperature planets, as these have the reddest $H - L'$ and $H - M$ colors. Such very low temperature planets can only be detected around the nearest stars, so it is for very nearby stars

that L' and M band observations make the most sense. According to the Burrows et al. (2003) models, the most sensitive H-regime observations made to date (those of Lafrenière et al. (2007)) would have set better mass limits than our observations around all of our survey targets except the very nearest objects, such as ϵ Eri and 61 Cyg. At present, the H-regime delivers far the best planet detection prospects for most stars.

However, as larger telescopes are built and longer planet detection exposures are attempted, the sensitivity at all wavelengths will increase. This means that low-temperature planets, with their red IR colors, will be detectable at large distances, and the utility of the L' and especially the M bands will increase. In Figure 21 we show the minimum detectable planet mass for hypothetical stars at 5 and 10 pc distance as a function of the increase over current sensitivity in the H, L', and M bands. We have taken current sensitivity to be $H = 23.0$ (i.e., Lafrenière et al. (2007)), $L' = 16.5$, and $M = 13.5$ (i.e., the present work, scaled to an 8m telescope such as Lafrenière et al. (2007) used). These are background limits, not applicable close to bright stars. Based on Heinze et al. (2008), we believe the L' and M bands will do even better relative to H closer to the star where observations are no longer background limited. We have deliberately chosen the characteristics of the hypothetical stars to be less good than the best available planet search candidates, so that in each case a number of stars closer and younger than each example actually exist.

Figure 21 illustrates two very important points. First, with a relatively minor increase of 1-1.5 mag in sensitivity, the M band will be sensitive to considerably lower-mass planets around stars within 5 pc than can be detected with H band observations, even if the H band sensitivity increases the same amount. Second, the advantage of the M band decreases with increasing distance, but as larger telescopes and longer exposures increase sensitivities to 2.5 mag above present levels, the M band will be superior to H out to 10 pc. In fact, with an increase of 3 mag, M band will surpass H out to 25 pc. All this applies to background-limited observations: close to bright stars, the relative utility of the M band should be even higher. Figure 21 also suggests that the M band is considerably more promising than L'. Note that the predicted supression of flux in the M band due to elevated levels of CO (Leggett et al. 2007; Reid & Cruz 2002) will not apply to planets at the low temperatures relevant for Figure 21. Though they are at present far surpassed in sensitivity by H-regime observations for all but the nearest stars, the L' and especially the M bands hold considerable promise for the future.

9. Conclusion

We have surveyed unusually nearby, mature star systems for extrasolar planets in the L' and M bands using the Clio camera with the MMT AO system. We have developed a sophisticated image processing pipeline for data from this camera, including some interesting innovations. We have carefully and rigorously analyzed our sensitivity. Speckle residuals surrounding bright stars can introduce serious bias into some popular sensitivity estimators, but we have developed two that are not subject to this bias. Blind tests involving fake planets inserted in raw data are the

best way to confirm the validity of any sensitivity estimator, and should be included in all future planet-search publications. By extensive use of such tests, we established a definitive significance vs. completeness relation for planets in our data, which we then used in Monte Carlo simulations to constrain planet distributions.

We discovered a physically orbiting $\sim 0.15 M_{\odot}$ binary companion at a projected separation of 80 AU from the star GJ 3876. However, we did not detect any planets. Our constraints on the distribution of planets from this null result are similar to constraints placed by Kasper et al. (2007) and Biller et al. (2007), but less tight than those of Nielsen et al. (2008) and especially Lafrenière et al. (2007). However, we have surveyed a more nearby, older set of stars than any previous survey, and have therefore placed constraints on a more mature population of planets. Also, we have confirmed that a paucity of giant planets at large separations from sun-like stars is robustly observed at a wide range of wavelengths.

The best current H regime observations, those of Lafrenière et al. (2007), would attain sensitivity to lower mass planets than did our L' and M band observations for all of our survey targets except those lying within 4 pc of the Sun. However, as larger telescopes are built and longer exposures are attempted, the sensitivity of M band observations may be expected to increase at least as fast as that of H band observations (in part because M band detectors are currently a less mature technology). A modest increase from current sensitivity levels, even if paralleled by an equal increase in H band sensitivity, would render the M band the wavelength of choice for extrasolar planet searches around a large number of nearby stars.

10. Acknowledgements

This research has made use of the SIMBAD online database, operated at CDS, Strasbourg, France, and the VizieR online database (see Ochsenbein et al (2000)).

We have also made extensive use of information and code from Press et al. (1992).

We have used digitized images from the Palomar Sky Survey (available from http://stdatu.stsci.edu/cgi-bin/dss_form), which were produced at the Space Telescope Science Institute under U.S. Government grant NAG W-2166. The images of these surveys are based on photographic data obtained using the Oschin Schmidt Telescope on Palomar Mountain and the UK Schmidt Telescope.

Facilities: MMT, 61" Kuiper

REFERENCES

Barrado y Navascués, D. 1998, A&A, 339, 831

Baraffe, I., Chabrier, G., Barman, T. S., Allard, F., & Hauschildt, P. H. 2003, A&A, 402, 701

Baraffe, I., Chabrier, G., Allard, F., Hauschildt, P. H. 1998, A&A, 337, 403

Biller, B. A., Close, L. M., Masciadri, E., Nielsen, E., Lenzen, R., Brandner, W., McCarthy, D., Hartung, M., Kellner, S., Mamajek, E., Henning, T., Miller, D., Kenworthy, M., & Kulesa, C. 2007, ApJS, 173, 143

Bouchy, F., Mayor, M., Lovis, C., Udry, S., Benz, W., Bertaux, J.-L., Delfosse, X., Mordasini, C., Pepe, F., Queloz, D., & Segransan, D. 2009, A&A, 496, 527

Bryden, G., Beichman, C. A., Trilling, D. E., Rieke, G. H., Holmes, E. K., Lawler, S. M., Stapelfeldt, K. R., Werner, M. W., Gautier, T. N., Blaylock, M., Gordon, K. D., Stansberry, J. A., & Su, K. Y. L. 2006, ApJ, 636, 1098

Burrows, A., Sudarsky, D., & Lunine, J. I. 2003, ApJ, 596, 578

Butler, R. P., Wright, J. T., Marcy, G. W., Fischer, D. A., Vogt, S. S., Tinney, C. G., Jones, H. R. A., Carter, B. D., Johnson, J. A., McCarthy, C., & Penny, A. J. 2006, ApJ, 646, 505.

Cohen, M., Walker, R. G., Michael, J. B., & Deacon, J. R. 1992, AJ, 104, 1650

Cox, A. N. 2000, Allen's Astrophysical Quantities (Fourth Edition; New York, NY: Springer-Verlag New York, Inc.)

Cumming, A., Butler, R. P., Marcy, G. W., Vogt, S. S., Wright, J. T., & Fischer, D. A. 2008, PASP, 120, 531.

Cutri, R., Skrutskie, M., van Dyk, S., Beichman, C., Carpenter, J., Chester, T., Cambresy, L., Evans, T., Fowler, J., Gizis, J., Howard, E., Huchra, J., Jarett, T., Kopan, E., Kirkpatrick, J., Light, R., Marsh, K., McCallon, H., Schneider, S., Stiening, R., Sykes, M., Weinberg, M., Wheaton, W., Wheelock, S., & Zacarias, N. 2003, 2MASSS All Sky Catlog of point sources (The IRSA 2MASS All-Sky Point Source Catalog, NASA/IPAC Infrared Science Archive. http://irsa.ipac.caltech.edu/applications/Gator/)

Favata, F., Micela, G., Sciortino, S., & D'Antona, F. 1998, A&A, 335, 218

Fischer, D. 1998, PhD Thesis entitled **Lithium Abundances in Field K Dwarfs**, University of California Santa Cruz

Fischer, D. A. & Valenti, J. 2005, ApJ, 622, 1102

Freed, M., Hinz, P., Meyer, M., Milton, N., & Lloyd-Hart, M. 2004, Proc. SPIE, 5492, 1561

Gomes, R., Levison, H., Tsiganis, K., & Morbidelli, A. 2005 Nature, 435, 466

Heinze, A. N., Hinz, P. M., Kenworthy, M., Miller, D., & Sivanandam, S. 2008, ApJ, 688, 583

Hinz, P., Heinze, A., Sivanandam, S., Miller, D., Kenworthy, M., Brusa, G., Freed, M., & Angel, J. 2006, ApJ, 653, 1486.

Hubeny, I. & Burrows, A. 2007, ApJ, 668,1248

Hünsch, M., Schmitt, J., Sterzik, M. & Voges, W. 1998, Astron. Astrophys. Suppl. Ser. 135, 319

Juric, M. & Tremaine, S. 2007, ArXiv e-prints, astro-ph/0703.0160

Karatas, Y., Bilir, S., & Schuster, W. 2005, MNRAS, 360, 1345

Kasper, M., Apai, D. Janson, M. & Brandner, W. 2007, A&A, 472, 321

Kenworthy, M., Codona, J., Johanan, L., Hinz, P., Angel, J., Heinze, A., & Sivanandam, S. 2007, ApJ, 660, 762

King, J., Villarreal, A., Soderblom, D., Gulliver, A., & Adelman, S. 2003, ApJ, 125,1980

Lafrenière, D., Doyon, R., Marois, C., Nadeau, D., Oppenheimer, B., Roche, P., Rigaut, F., Graham, J., Jayawardhana, R., Johnstone, D., Kalas, P., Macintosh, B., & Racine, R. 2007, ApJ, 670, 1367

Leggett, S., Saumon, D., Marley, M., Geballe, T., Golimowksi, D., Stephens, D., & Fan, X. 2007, ApJ, 655, 1079

López-Santiago, J., Montes, D., Crespo-Chac/'on, I., & Fernández-Figueroa, M. J. 2006, ApJ, 643, 1160

Lowrance, P., Becklin, E., Schneider, G., Kirkpatrick, J., Weinberger, A., Zuckerman, B., Dumas, C., Beuzit, J., Plait, P., Malumuth, E., Heap, S., Terrile, R., & Hines, D. 2005, AJ, 130, 1845

Marley, M. S., Fortney, J. J., Hubickyj, O., Bodenheimer, P., & Lissauer, J. J. 2007, ApJ, 655, 541

Marois, C., Lafrenière, D., Doyon, R., Macintosh, B., & Nadeau, D. 2006, ApJ, 641, 556

Marois, C., Macintosh, B., Barman, T., Zuckerman, B., Song, I., Patience, J., Lafrenière, D., & Doyon, R. 2008, Science, 322, 1348

Masciadri, E.; Mundt, R.; Henning, Th.; Alvarez, C.; & Barrado y Navascués, D 2005, ApJ, 625, 1004

Montes, D., López-Santiago, J., Fernaández-Figueroa, M., & Gálvez, M. 2001, A&A, 379, 976

Mugrauer, M., Neuhaeuser, R., Guenther, E. W., Hatzes, A. P., Huelamo, N., Fernandez, M., Ammler, M., Retzlaff, J., Koenig, B., Charbonneau, D. Jayawardhana, R., & Brandner, W. 2004, A&A, 417, 1031

Nielsen, E. L., Close, L. M., Biller, B. A., Masciadri, E., & Lenzen, R. 2008, ApJ, 674, 466

Ochsenbein, F., Bauer, P. & Marcout, J. 2000, ApJS, 143, 23O

Potter, D., Cushing, M., & Neuhauser, R. 2003, csss, 12, 689

Perryman, M., Lindegren, L., Kovalevsky, J., Hog, E., Bastian, U., Bernacca, P., Creze, M., Donati, F., Grenon, M., Grewing, M., Van Leeuwen, F., Van Der Marel, H., Mignard, F., Murray, C., Le Poole, R., Schrijver, H., Turon, C., Arenou, F., Froeschle, M., & Peterson, C. 1997, A&A, 323, L49

Press, W. H., Teukolsky, S.A., Vetterling, W. T., & Flannery, B. P. 1992, Numerical Recipes in C (Second Edition; New York, NY: Cambridge University Press)

Reid, I. & Cruz, K. 2002, AJ, 123, 466

Sivanandam, S., Hinz, P., Heinze, A., & Freed, M. 2006, Proc. SPIE, 6269, 27

Song, I., Zuckerman, B., & Bessell, M. 2003, ApJ, 599, 342

van Dokkum, P. G. 2001, PASP, 113, 1420

Wichmann, R., Schmitt, J., & Hubrig, S. 2003, A&A, 399, 983

Wichmann, R. & Schmitt, J. 2003, MNRAS, 342, 1021

Zuckerman, B., Song, I., Bessell, M., & Webb, R. 2001, ApJ, 562, L87

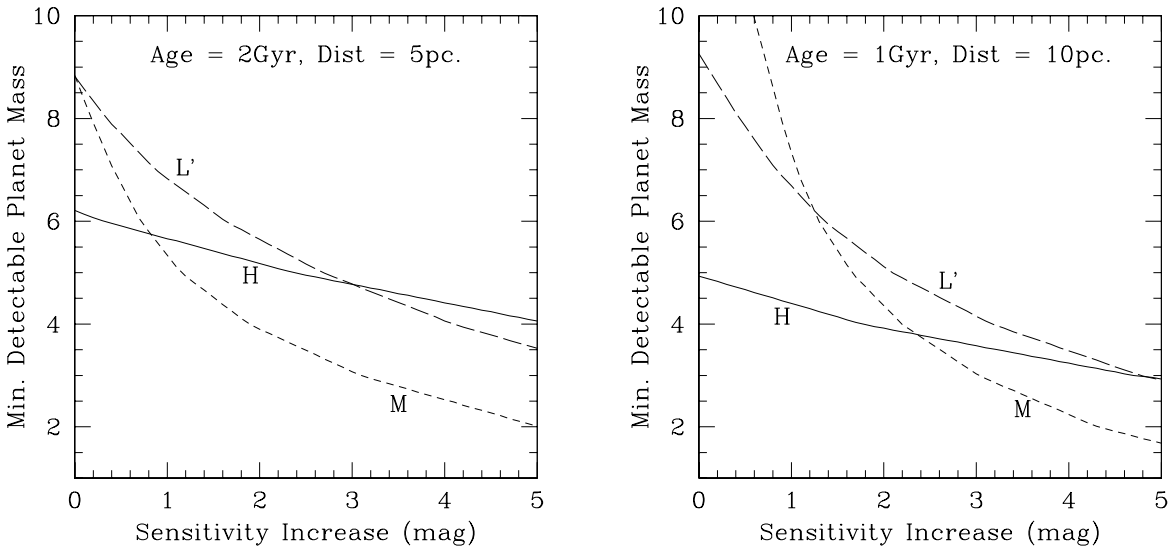

Fig. 21.— Minimum detectable planet mass in units of MJ for stars at 5pc (left) and 10pc (right), in the H, L', and M bands, as a function of increase over current sensitivity. We have taken current sensitivities to be $H = 23.0$, $L' = 16.5$, and $M = 13.5$. Modest increases over current sensitivities will render the M band very promising relative to shorter wavelengths, especially for nearby stars.